Geotechnical Extreme Events Reconnaissance Association
www.geerassociation.org

GEOTECHNICAL ENGINEERING RECONNAISSANCE OF THE 2022 CHIHSHANG EARTHQUAKE SEQUENCE

Version 1.0; April 2024

Editors: GEER Team Members: Domniki Asimaki (Caltech), H. Benjamin Mason (OSU)

DOI: 10.18118/G65M23

Geotechnical Extreme Events Reconnaissance Association
Report No. GEER- 083
April 5, 2024

Contributing Authors (in Alphabetical Order):

GEER team members: Domniki Asimaki (Caltech), H. Benjamin Mason (OSU) (team leads)

Adda Athanasopoulos-Zekkos (UCB), Trevor Carey (UBC), Fernando E. Garcia (UM), Brian Gray (LCI), Grigorios Lavrentiadis (Caltech), and Chukwuebuka C. Nweke (USC)

Other Contributors (not in Alphabetical Order):

NCREE (NARLabs): Chung-Che Chou (Director General), Chiun-Lin Wu (Deputy Director General), Zheng-Kuan Lee, Wei-Kuang Chang, Kuan-Yu Chen, Shih-Jung Lin, Chi-Hao Lin, Che-Min Lin

National Chi Nan University: Kuo-lung Wang (Professor), Jun-tin Lin, Yi-hsuan Lee

Acknowledgements

The work of the GEER Association is based in part on work supported by the National Science Foundation through the Geotechnical Engineering Program under Grant No. CMMI-1266418. Any opinions, findings, and conclusions or recommendations expressed in this material are those of the authors and do not necessarily reflect the views of the NSF. The GEER Association is made possible by the vision and support of the NSF Geotechnical Engineering Program Directors: Dr. Richard Fragaszy and the late Dr. Cliff Astill. GEER members also donate their time, talent, and resources to collect time-sensitive field observations of the effects of extreme events.

The GEER reconnaissance was co-led by Domniki Asimaki (Caltech) and H. Benjamin Mason (Oregon State University) and included team members Adda Athansopoulos-Zekkos (University of California, Berkeley), Trevor Carey (University of British Columbia), F. Estefan Garcia (University of Michigan), Brian Gray (Lettis Consultants International), Grigorios Lavrentiadis (Caltech), and Chukwuebuka Nweke (University of Southern California).

Our in-country partners helped ensure a smooth and productive reconnaissance effort. In particular, we thank NCREE for their generous time and effort that made this mission possible. We specifically would like to thank: Chung-Che Chou (Director General), Chiun-Lin Wu (Deputy Director General), Zheng-Kuan Lee, Wei-Kuang Chang, Kuan-Yu Chen, Shih-Jung Lin, Chi-Hao Lin, and Che-Min Lin. They helped with our travel to and within Taiwan and donated their time and expertise in the field to help us with the reconnaissance efforts. We would also like to thank members from the National Chi Nan University, who joined us in the field to perform aerial surveys using structure-for-motion and lidar drones: Kuo-lung Wang, Jun-tin Lin, and Yi-hsuan Lee. The government of Taiwan was very supportive of our travel and issuing our research permits. Many other people helped behind the scenes, and we would like to thank everyone who helped make our mission a collective success.

Lastly, the GEER team would like to thank the GEER Steering Committee and in particular David Frost and Elliot Nichols (Georgia Tech) for providing us with abundant support, guidance, and contacts during the reconnaissance effort.

Executive Summary

The Chishang events nucleated on the high-angle, west-dipping Central Range Fault (CRF), which is blind in the south, and was not in the official active faults map issued by the Taiwan Geological Survey. The M_w6.9 Chihshang mainshock occurred on 9/18/2022 at 14:44:15.2 (Taiwan Standard Time: GMT+08:00). The event was preceded by a foreshock of M_w6.5 on 9/17/2022 at 21:41:19.1. The U.S. GEER team, arrived in Taipei on 15 and 16 October 2022 and traveled to the affected region on 17 October; it included eight U.S.-based members, and was hosted and accompanied by a team of geologists, geotechnical engineers, and researchers from Taiwan's National Center for Research on Earthquake Engineering (NRCEE). Our main field observations focused on fault displacement induced damage in residential areas and directivity effects on bridges traversing the Longitudinal Valley. We observed that the Fuli and Yuli faults ruptured similarly to the 1951 sequence, with displacements of several tens of centimeters triggered on the Longitudinal Valley Fault (LVF). The largest offset observations were 1m left lateral slip / 1m uplift on the CRF hanging wall and 0.90m shortening on the LVR hanging wall. Strong fault normal velocity pulses in rupture direction (directivity pulses) and strong fault parallel pulses accommodating permanent slip resulted in catastrophic failure of bridges crossing the valley. The large velocity pulses caused bridge girder unseating, and triggered cascading failure in the piers. Despite the saturated nature of the loose sediments in the valley, we observed no ground failure at the bridge failure sites. Furthermore, preliminary nondestructive site characterization at the bridge damage sites suggested that the fundamental modes of the site conditions were too high to have contributed to the observed bridge damage in the form of double resonance (given that the period of the directivity pulses was long and so was the fundamental mode of the bridges). Ground failure in the form of liquefaction was not observed by the GEER reconnaissance team and site effects are unlikely to have contributed to the observed damage distribution along the valley. Lastly, the drone observations kindly captured by our collaborators at National Chi Nan University, were calibrated to cm-order error, and were invaluable for detailed rupture identification in areas too coarse for optical and radar imagery (e.g. the repeat rupture sites in Yuli and Fuli).

Table of Contents

1 INTRODUCTION

The **M**6.9 Chihshang, Taiwan earthquake occurred on 18 September 2022 at 14:44 local time. The strike-slip earthquake occurred on the north-south trending Central fault extending along the southeast coast of Taiwan. The U. S. Geological Survey (USGS) reports the earthquake's epicentral location at 23.138° N 121.344° E with an epicentral depth of 7.81 km. The fault ruptured north, leading to directivity effects. The earthquake caused bridge collapses and extensive surface fault rupture throughout the epicentral region; landslides were also observed, although the heavy rainfail immediately before and after the earthquake sequence made it hard to decipher the role of the earthquake as the dominant triggering or an add-on destabilizing mechanism of ground failure, already at near-failure as a result of saturation. Despite the epicentral region being an alluvial plain, surficial evidence of liquefaction was sparse to non-existent. Carey et al. (2023) documents some of the prior observations.

Notably, a **M**6.5 foreshock occurred on 17 September 2022 at 21:41 local time (approximately 17 hours before the **M**6.9 mainshock). The USGS reported the epicenter at 23.119° N 121.414° E with an epicentral depth of 8.61 km. The **M**6.5 foreshock undoubtedly caused damage before the **M**6.9 mainshock, and in some cases, may have pre-damaged bridges leading to collapse during the **M**6.9 mainshock. Notwithstanding the foregoing point, we focus our reporting efforts on the **M**6.9 mainshock, because we do not have access to many field observations between the two earthquakes to isolate the **M**6.5 foreshock damage. Figure 1.1 depicts the location of the September 2022 epicenters along with all historical earthquakes in the broader longitudinal valley region since 1900 with $M > 6$ and depth <30 km.

Taiwan's Central News Agency reported that the **M**6.9 mainshock killed one person and injured another 146. The earthquake also derailed a passenger train and collapsed the roof of the Dongli train station, causing major disruptions. We could not find reliable reports of the economic consequences of the earthquake.

The Geotechnical Extreme Events Reconnaissance (GEER) team, with support by the U.S. National Science Foundation (NSF), arrived in Taipei on October 15 and 16, and traveled to the affected region on October 17, 2022. We conducted five days of fieldwork. The GEER team, which included eight U.S.-based members, was hosted and accompanied by a team of geologists, geotechnical engineers, and researchers from Taiwan's National Center for Research on Earthquake Engineering (NCEER), as described in more detail below. *Given our close-knit field operations, we collectively refer to the U.S.-Taiwan field reconnaissance team as the GEER team herein.*

We originally split our team up into three sub-teams, to optimize our field campaign: 1) the bridge team, 2) the ground failure team, and 3) the surface fault rupture team. In the initial days, the ground failure team had trouble finding any evidence of liquefaction (a finding also reported by Taiwanese colleagues who travelled to the field immediately after the earthquake), and slope failure is so prevalent in southeast Taiwan, that it was difficult to segregate the slope failure mechanisms between seismic and gravity. Accordingly, the ground failure team split and joined the bridge and surface fault rupture teams. At the same time, we had a subgroup investigating

the recorded ground motions. We have arranged the report with respect to the observations of the preceding sub-teams. Our entire reconnaissance team bridges a wide range of expertise, so membership of the sub-teams remained fluid during our field campaign. A bird's eye view of the sites that our GEER mission visited is shown in Figure 1.2. These sites are outlined in more detail in forthcoming chapters of this report.

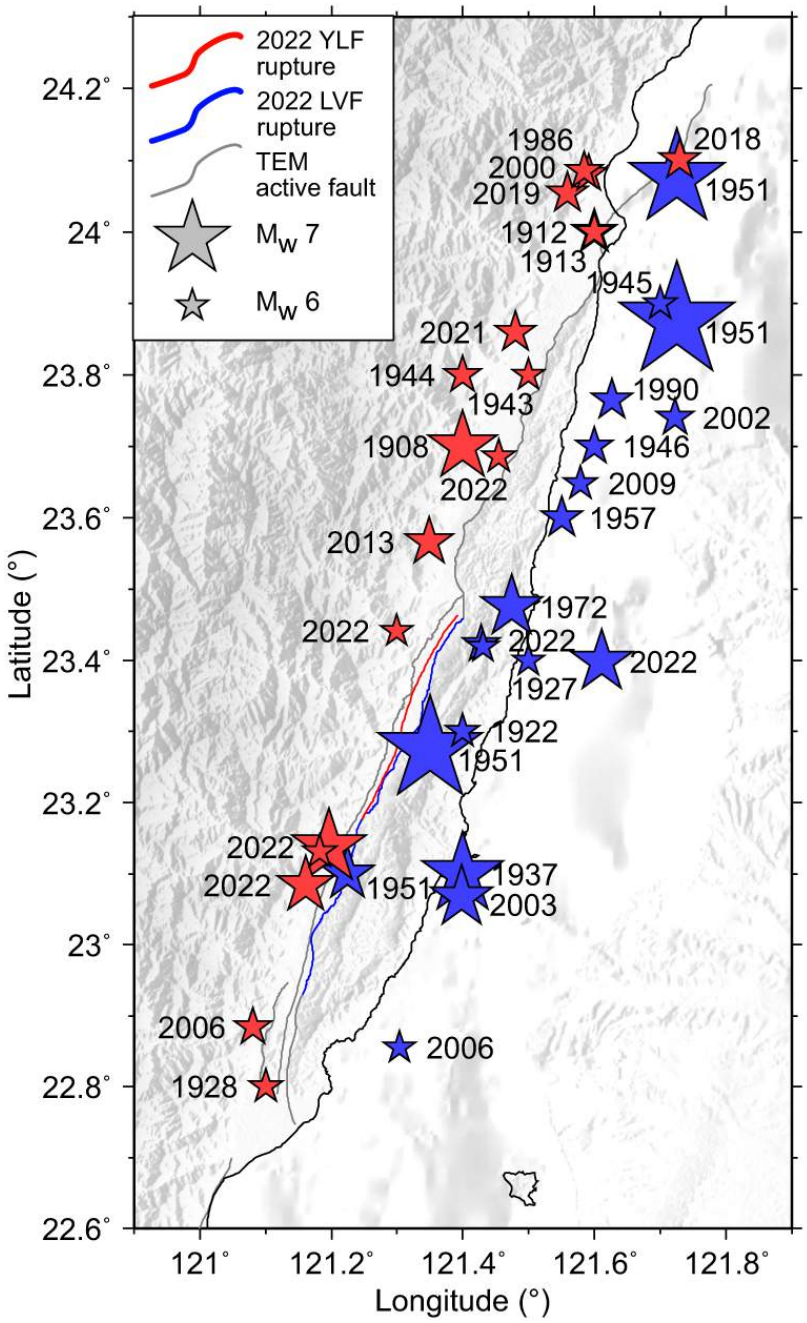

Figure 1.1 Spatial distribution of historical earthquakes since 1900 with $M > 6$ and depth <30 km. Red and blue stars mark earthquakes attributed to the CRF and LVF, respectively. Red and blue lines are the 2022 surface ruptures along the Yuli fault and the LVF. Gray lines represent other active faults in the Taiwan Earthquake Model (modified from Tang et al, 2023).

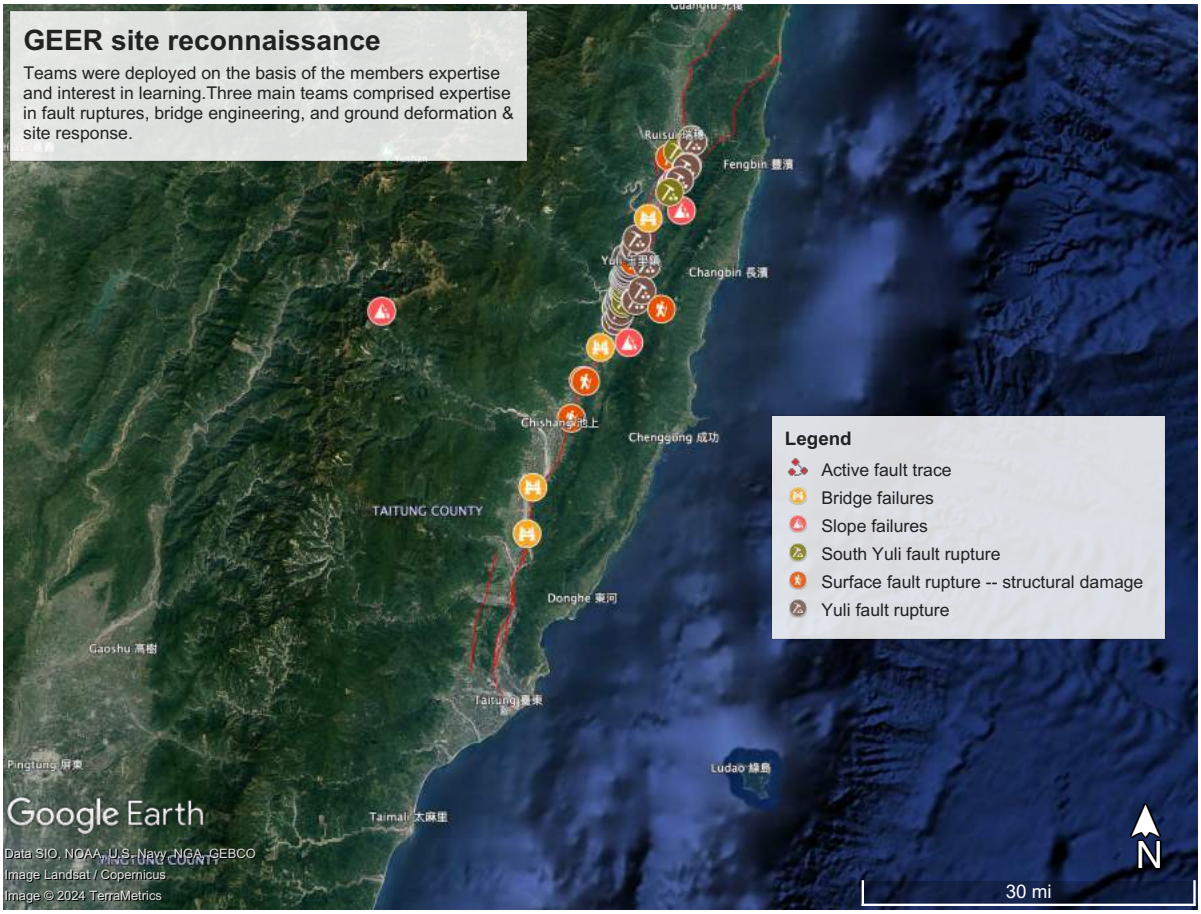

Figure 1.2 Bird's eye view of the GEER mission, categorized by class of failures that we focused on.

REFERENCES

Carey, T. J., Mason, H. B., Asimaki, D., Athanasopoulos-Zekkos, A., Garcia, F. E., Gray, B., ... & Nweke, C. C. (2023). The 2022 Chihshang, Taiwan, Earthquake: Initial GEER Team Observations. *Journal of Geotechnical and Geoenvironmental Engineering*, *149*(5), 02823002.

Tang, C. H., Lin, Y. N., Tung, H., Wang, Y., Lee, S. J., Hsu, Y. J., ... & Chen, H. Y. (2023). Nearby fault interaction within the double-vergence suture in eastern Taiwan during the 2022 Chihshang earthquake sequence. *Communications Earth & Environment*, *4*(1), 333.

2 NON-INVASIVE SITE CHARACTERIZATION TESTING

This section documents the GEER/NCREE team's temporary seismic instrument deployment efforts to acquire data for possible site characterization at bridge sites that experienced damage during the 2022 **M**6.5 and **M**6.9 earthquakes. The team, led by Chukwuebuka C. Nweke, deployed three 120-second Nanometric Trillium Compact Horizon Seismometers (3 component: 2 horizontals and 1 vertical) at the eastern half of the Luntian Bridge, and the western and eastern end of the Gaoliao Bridge to passively collect recordings of ambient vibrations. Unfortunately, due to demolition activities, spatial distribution of damage debris, repair efforts, and active river flow, it was not possible to configure an optimal testing layout. However, effort was made to approximate a triangular array to account for azimuthal effects.

2.1 Ground Conditions at Testing Locations

The Tropic of Cancer (latitude of 23.4394 degrees North or 23° 26'N) crosses the island of Taiwan and can serve as the northern boundary of the region adversely affected by the earthquake sequence.

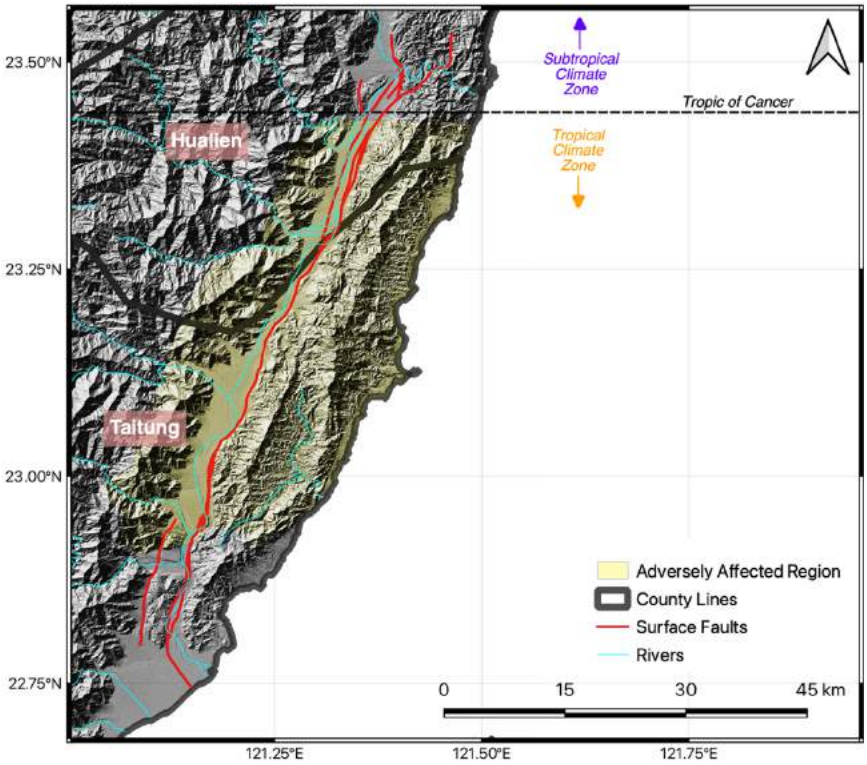

Figure 2.1 Summary map of region adversely affected by the **M**6.9 and **M**6.5 earthquakes, the counties, and known fault locations.

Figure 2.1 also indicates that the region affected lies in a tropical climate zone that experiences heavy rainfall which is enhanced by seasonal monsoons and surrounding mountains. The existence of this climate type in this tectonic environment (described in Chapter 4) leads to geomorphic processes (weathering, transport, and deposition) that make for a highly active landscape evolution. The rivers act as the major conduit of relief for the resulting land and water movement. For this reason, the bridge locations where testing was conducted had highly variable

ground surface conditions consisting of fine sands and silts mixed in with numerous gravels and cobbles of a wide range of sizes. This was overlaid by a layer of clay and very fine silt that was washed away at random spots by river flow to expose the sandy-silty-gravel/cobble mix. At the same time, due to the damage sustained by the bridges an appreciable portion of the ground surface was covered by demolished bridge deck material which consisted of fractured concrete blocks of varying sizes mixed with rebar.

2.2 Sensor/Seismometers and Deployment Method

The temporary deployment of sensors requires systematic setup practices to encourage repeatability. For this, our procedures align with those detailed in the SESAME guidelines. When possible, the sensors were partially buried to improve ground coupling. Alternatively, when the ground could not be dug with a shovel the sensors were placed on the ground surface. In all cases, the sensors were covered with buckets to prevent the influence of wind. The trillium compact horizon seismometers have a natural period of 120-seconds therefore they may take a longer amount of time to stabilize. However, these sensors have the capability to decrease stabilization time by engaging a short period mode (akin to the 20-seconds sensor equivalents). For these deployments, this feature was not used. This is not an issue for long testing durations, but it could be for shorter testing durations. The sensors used at the bridges were deployed for about 1.25 – 2.5 hours, and the variations of testing duration was due to environmental constraints (weather changes due to rain), schedule of visit (time allotted to each site or changes in schedule), or time of day (available daylight). Figure 2.2 shows the different pieces of equipment needed for one sensor operation. This includes the sensor itself, the digitizer that captures the recorded vibrations, the battery to power the device, the cords to connect the digitizer to the sensor and battery, and the containment box which houses all the components.

2.3 Luntian Bridge Testing

Access to the riverbed and the bridge columns was achieved through an access road approximately 0.4 km south of the bridge along the eastern levee. The three seismometers were deployed in a triangular configuration with two sensors located in between bridge columns (one end of the triangular array is parallel with the span of the bridge). Figure 2.3 shows the layout of the sensors. Here LTB-USC1 was located at approximately 33 meters in the southwest direction perpendicular to the bridge span point that is approximately 90 meters from the levee crest along said span. LTB-USC2 was located immediately adjacent to the bridge span approximately 67 meters from the levee crest. LTB-USC3 was located approximately 45 meters away from LTB-USC2 along the bridge span to the northwest direction. Figure 2.4 shows the physical setup at each sensor location on the day of deployment as well as the ground conditions. At this location, these sensors were placed on the ground surface.

The intention of the reconnaissance team was to record ambient vibration at portions of the bridge that were structurally intact and portions that failed due to the earthquake ground motions. Unfortunately, the debris that covered the area with the failed portions of the bridge created a huge safety issue due to the amount of protruding rebar and unstable fractured blocks. As a result, sensor deployment was only possible in the portions of the bridge that was still intact. In addition, the duration of testing was disrupted by the emergence of rain clouds that was migrating towards the river, which lead to concerns about safety with regards to potential river flow elevation changes. In all, approximately 1.75 hours or data was collected between the three sensors.

Figure 2.2. Necessary components/equipment for the operation of one seismometer

Figure 2.3. Layout of the temporary seismometer deployment at Luntian bridge. Shows the configuration of the Triangular array, highlighting the distances between the sensors, the location of the eastern levee footprint, and the bridge.

Figure 2.4. Photo of sensor setup at Luntian bridge. (a) LTB-USC1; (b) LTB-USC2; (c) LTB-USC3.

2.4 Gaoliao Bridge Testing

Western End

Access to this portion of the bridge was achieved through the stairs at the end of the road to the north. The stairs are located on the levee at the point before it curves to the west and travels parallel to the bridge. There was active demolition equipment being operated at the time of arrival, but this was concluded just before the beginning of the testing duration. The amount of debris that covered the site made it difficult to construct a proper triangular array, but an attempt was made nonetheless. Figure 2.5 shows the sensor array configuration at the western end of Gaoliao bridge. GBW-USC1 was located north of the bridge span, approximately 18 meters from the end of the bridge approach abutment. GBW-USC2 was located immediately south of the bridge, approximately 82 meters east of the bridge abutment along the span. GBW-USC3 was located close to the access entrance stairs, approximately 26 meters north of the bridge and 14 meters west of the riverbank. Figure 2.6 shows the physical setup at each sensor on the day of deployment as well as the ground conditions. These sensors at this location were partially buried because of the silty-sandy clayey soil that was easy to dig. The duration of testing at this location was approximately 2.5 hours between the three sensors.

Eastern End

Access to the testing location was achieve through the levee steps immediately west of the abutment that serves as the end of the earthen built bridge approach. Similar to the western end of the bridge, the site was blanketed with debris consisting of fractured bridge deck concrete material mixed with protruding rebar which made it difficult to construct a proper triangular array. Fortunately, the demolition equipment used to break down the bridge deck traversed a path on both sides of the rubble that we used as locations to setup a sensor triangular array as best we could. Figure 2.7 shows the sensor configuration at the eastern end of Gaoliao bridge. Sensors GBE-USC1 and GBE-USC2 were located adjacent to the bridge, with the leg of the triangle

connecting both sensors running parallel to the bridge span. GBE-USC1 and GBE-USC2 were approximately 101 meters and 190 meters, respectively, from the eastern bridge abutment. GBE-USC3 was approximately 28 meters north of the bridge at a point that was approximately 27 meters west of GBE-USC1. Figure 2.8 shows the physical setup at each sensor on the day of deployment as well as the ground conditions. Like the western end of the bridge, the sensors at this location were also partially buried because the silty-sandy clayey soil was easy to dig. On the other hand, the duration of testing at this location was approximately 1.08 hours between the three sensors. The difference in data time length is due to the fact that we reached this site later in the evening and we underestimated the amount of sunlight left in the day.

Figure 2.5. Layout of the temporary seismometer deployment at the western end of Gaoliao bridge. Shows the configuration of the semi-triangular array, highlighting the distances between the sensors, the location of the access point, the abutment, and the bridge.

Figure 2.6. Photo of sensor setup at Gaoliao bridge (Western end). (a) GBW-USC1; (b) GBW-USC2; (c) GBW-USC3.

Table 2.1 provides a summary of the installation/setup and configuration information on all the sensor and location combinations. It details the dates of testing, the coordinates to the sensor locations at each testing site, the start and end time corresponding to the configuration and termination of testing duration, the system (digitizer) and sensor temperature, the internal mass balance values at the beginning and end of testing, as well as the recorded elevation (by the digitizer) and the length of the ambient vibration record. Regarding weather conditions, for the first day of testing there was no rain but pervasive cloud cover above us in the valley and surrounding rain clouds in the mountains. The second day of testing was sunny with clear skies, which changed into cloud cover by the evening testing period.

Table 2.1. Installation, setup, and configuration details for the temporary sensor deployments at the bridge sites.

Site ID	Date	Sensor Name	Latitude	Longitude	Start Time UTC	Start Time Taiwan ST	End Time UTC	End Time Taiwan ST
LTB-USC1	10/18/22	USC-1	23.216697	121.272022	1:38 AM	9:38 AM	3:33 AM	11:33 AM
LTB-USC2	10/18/22	USC-2	23.216842	121.272418	1:54 AM	9:54 AM	3:39 AM	11:39 AM
LTB-USC3	10/18/22	USC-3	23.217037	121.272027	2:11 AM	10:11 AM	3:50 AM	11:50 AM
GBW-USC1	10/20/22	USC-1	23.386320	121.338580	1:30 AM	9:30 AM	4:00 AM	12:00 PM
GBW-USC2	10/20/22	USC-2	23.385985	121.339233	1:46 AM	9:46 AM	4:08 AM	12:08 PM
GBW-USC3	10/20/22	USC-3	23.386263	121.339867	2:04 AM	10:04 AM	4:18 AM	12:18 PM
GBE-USC1	10/20/22	USC-1	23.385282	121.346010	8:20 AM	4:20 PM	9:35 AM	5:35 PM
GBE-USC2	10/20/22	USC-2	23.385353	121.345145	8:32 AM	4:32 PM	9:41 AM	5:41 PM
GBE-USC3	10/20/22	USC-3	23.385535	121.345752	8:42 AM	4:42 PM	9:46 AM	5:46 PM

Figure 2.7. Layout of the temporary seismometer deployment at the eastern end of Gaoliao bridge. Shows the configuration of the semi-triangular array, highlighting the distances between the sensors, the location of the access point, the abutment, and the bridge.

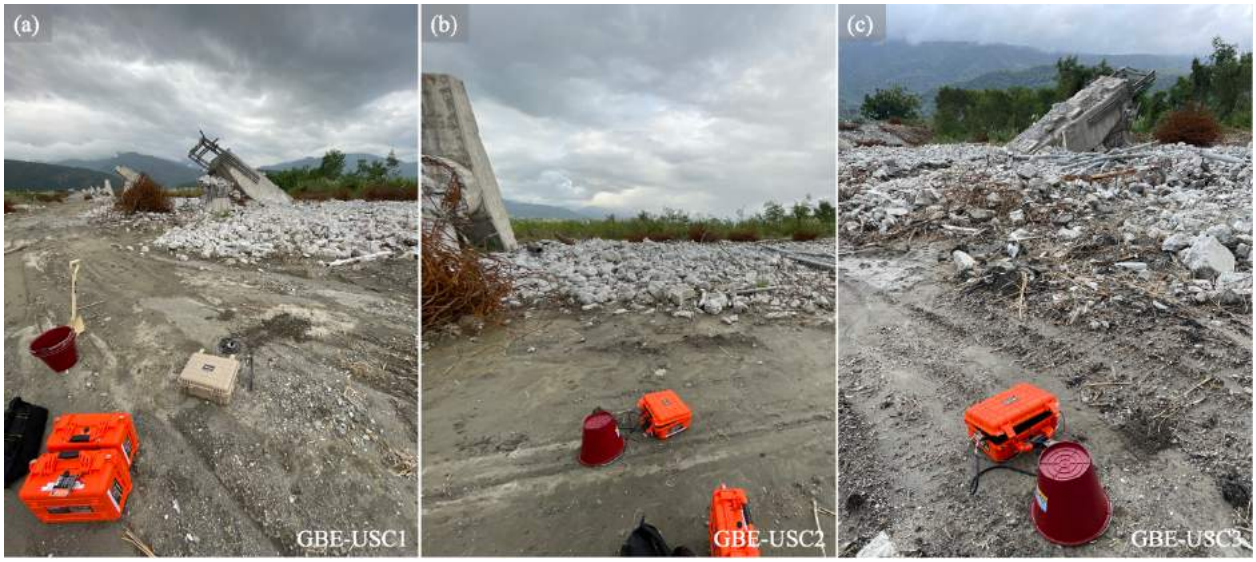

Figure 2.8. Photo of sensor setup at Gaoliao bridge (Eastern end). (a) GBE-USC1; (b) GBE-USC2; (c) GBE-USC3.

Table 2.1 (cont) Installation, setup, and configuration details for the temporary sensor deployments at the bridge sites.

Site ID	Length of Record (hr:min:sec)	Elevation (m)	System Starting Temp (℃)	Sensor Starting Temp (℃)	System Ending Temp (℃)	Sensor Ending Temp (℃)
LTB-USC1	1:53:15	224.9	21.9	22.5	25.8	26.4
LTB-USC2	1:44:09	216.7	20.8	22.5	23.7	25.3
LTB-USC3	1:38:37	218.6	22.4	23.0	24.3	24.8
GBW-USC1	2:29:39	122.8	21.5	22.1	29.1	27.1
GBW-USC2	2:20:50	123.0	21.7	22.8	29.0	28.5
GBW-USC3	2:12:59	109.2	24.2	24.6	30.1	29.3
GBE-USC1	1:13:56	105.5	27.5	27.5	25.4	26.9
GBE-USC2	1:08:39	101.1	28.3	28.4	25.7	26.0
GBE-USC3	1:03:42	104.6	28.2	28.6	26.2	26.3

Site ID	Starting Mass Position - W	Starting Mass Position - V	Starting Mass Position - U	Ending Mass Position - W	Ending Mass Position - V	Ending Mass Position - U
LTB-USC1	0.69	-0.01	0.10	0.62	-0.07	0.01
LTB-USC2	0.60	0.57	0.50	0.54	0.52	0.44
LTB-USC3	0.09	1.46	0.36	0.06	1.46	0.31
GBW-USC1	0.65	0.31	-0.12	0.56	0.23	-0.22
GBW-USC2	0.83	0.37	0.44	0.75	0.27	0.35
GBW-USC3	0.58	1.15	0.13	0.51	1.08	0.05
GBE-USC1	0.59	-0.06	-0.13	0.61	-0.04	-0.11
GBE-USC2	0.80	0.09	0.34	0.87	0.13	0.41
GBE-USC3	0.44	1.24	-0.13	0.49	1.29	-0.07

2.5 Data Processing for Site Characterization Using mHVSR

The ambient vibrations recorded at the three site locations (Luntian, Gaoliao west, and Gaoliao east) were used to estimate subsurface site features via microtremor horizontal-to-vertical spectral ratio (mHVSR). mHVSR is the ratio of the horizontal-to-vertical Fourier amplitude spectra (FAS) derived from ambient vibration recordings on a three-component seismometer. It provides an estimate of the site fundamental mode resonance frequency (site period). This is achieved by partitioning the ambient vibration recording into specific window lengths, rejecting anomalous

windows, filtering the record to highlight the signal, calculating the FAS and applying smoothening, then combining both horizontal components and subsequently taking the ratio to the vertical component. Detailed explanation of the processing method and calculations used for mHVSR are provided in Molnar et al. 2022. We employ the HVSR software hvsrProc to process the data and calculate the curve. This analysis was repeated using HVSRPy which showed nearly identical results.

For the ambient vibration data acquired, the following list details some of the processing information (Table 2.2 provides more information related to the window length and window selection per sensor at each location):

- Sampling frequency was 200 Hz.
- No detrend was applied to the record.
- A Tukey taper type was applied with a front and end taper width of 5%.
- A Butterworth filter was applied to the entire record (not the windowed record) with the high pass corner frequency set to 0.042 Hz.
- The FAS for the three components was smoothed using a Konno-Ohmachi filter with a smoothing constant of 40.
- The two horizontal components were combined using a geometric mean.

Table 2.2. Window length and window selection for each sensor at the three testing locations.

Site ID	Record Duration (min)	Time Window Length (sec)	Number of Windows (Total)	Number of Windows (Selected)
LTB-USC1	75.0	300	15	8
LTB-USC2	75.0	300	15	9
LTB-USC3	30.0	150	12	7
GBW-USC1	154.7	300	30	17
GBW-USC2	144.9	300	28	19
GBW-USC3	136.5	300	27	10
GBE-USC1	78.8	300	15	4
GBE-USC2	71.5	300	14	4
GBE-USC3	66.5	300	13	4

Figure 2.9 shows the resulting mHVSR curves. The sensors at Luntian bridge indicate a site period at approximately 0.1 – 0.15 seconds (6.5 -10 Hz). The western and eastern end of Gaoliao bridge show similar estimate range of site period at approximately 0.2 – 0.67 seconds (1.5 – 5 Hz). The values of the site period/fundamental resonant frequencies are also detailed in Table 2.3.

Table 2.3. The fundamental resonant frequencies/site period for the three sensors at each bridge test site.

Site ID	Fundamental Frequency, f_0 (Hz)	Site Period, T_0 (sec)
LTB-USC1	6.47	0.15
LTB-USC2	8.81	0.11
LTB-USC3	11.10	0.09
GBW-USC1	1.59	0.63
GBW-USC2	2.71	0.37
GBW-USC3	2.78	0.36
GBE-USC1	2.49	0.40
GBE-USC2	2.67	0.37
GBE-USC3	5.01	0.20

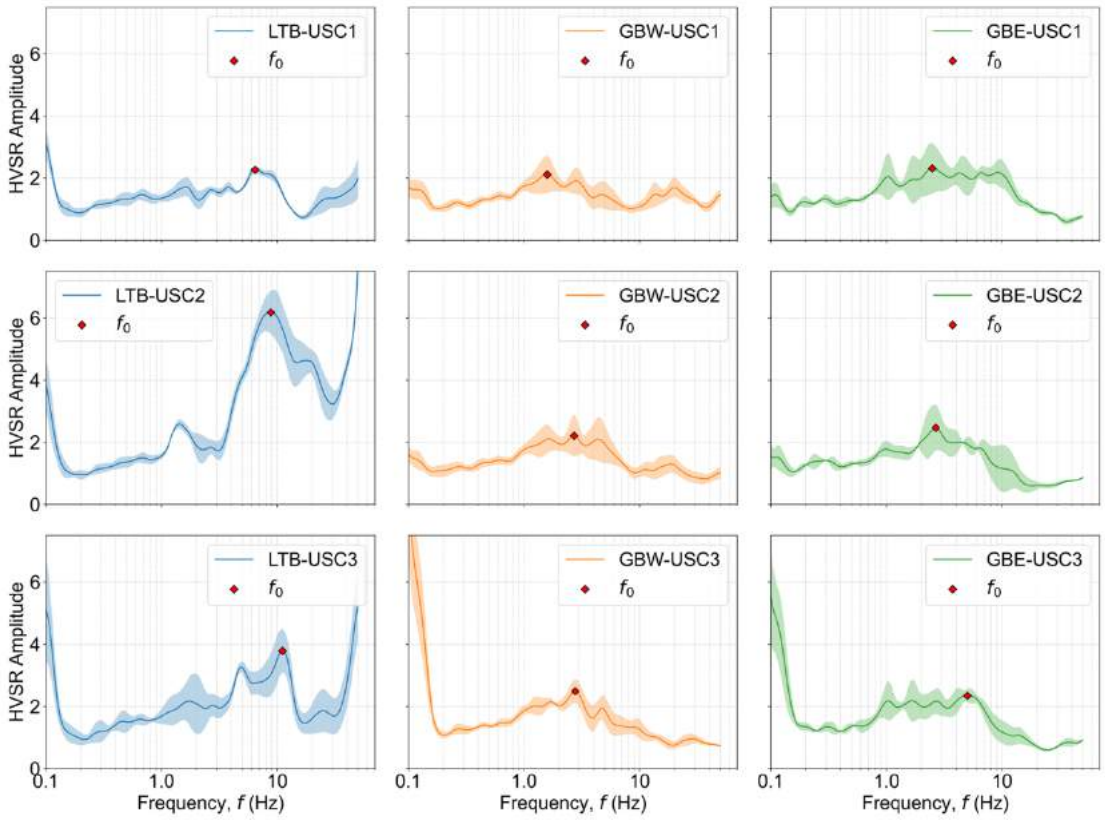

Figure 2.9. Plot of mean mHVSR curves derived from the recorded ambient vibrations at the bridge locations. The shaded regions around the mean curve (solid lines) represent ± 1 standard deviation. The red diamond indicates the estimated fundamental site frequency taken as the maximum amplitude peak within the range of 0.2 – 30 Hz.

Overall, the data gathered during the reconnaissance efforts provides a first attempt to characterize the subsurface site conditions at these bridge sites that collapsed during the earthquakes. *All sites characterized appear to have very high fundamental modes and, when* analyzed in conjunction with the long period near fault pulses that appear to have triggered the bridge failures, we are inclined to believe that site effects played a minimal, if any, role in the observed catastrophic damage of the longitudinal valley transportation infrastructure.

REFERENCES

Acerra, C., Aguacil, G., Anastasiadis, A., Atakan, K., Azzara, R., Bard, P. Y., ... & Zacharopoulos, S. (2004). Guidelines for the implementation of the H/V spectral ratio technique on ambient vibrations measurements, processing and interpretation. European Commission–EVG1-CT-2000-00026 SESAME.

Chen, H., Lin, G. W., Lu, M. H., Shih, T. Y., Horng, M. J., Wu, S. J., & Chuang, B. (2011). Effects of topography, lithology, rainfall and earthquake on landslide and sediment discharge in mountain catchments of southeastern Taiwan. Geomorphology, 133(3-4), 132-142.

Konno, K., & Ohmachi, T. (1998). Ground-motion characteristics estimated from spectral ratio between horizontal and vertical components of microtremor. Bulletin of the Seismological Society of America, 88(1), 228-241.

Molnar, S., Sirohey, A., Assaf, J., Bard, P. Y., Castellaro, S., Cornou, C., ... & Yong, A. (2022). A review of the microtremor horizontal-to-vertical spectral ratio (MHVSR) method. Journal of Seismology, 26(4), 653-685.

Vantassel, J. (2020). jpvantassel/hvsrpy: latest (Concept). Zenodo. http://doi.org/10.5281/zenodo.3666956

Wang, P. wltcwpf/hvsrProc: First release (Version v1.0.0). Zenodo. http://doi.org/10.5281/zenodo.4724141

3. GROUND MOTIONS & TECTONIC OFFSET

3.1 Tectonic and Geologic Setting

The island of Taiwan rests on the eastern margin of the stable Eurasian plate, a product of collision of the Philippine Sea and Eurasian plates (Figure 3.1). The active collisional nature of the Eurasian\Philippine Sea plate boundary produced the Taiwan orogen over the past few million years. Using 1990-1995 global positioning system (GPS) data from the Taiwan GPS network, Yu et al. (1997) show the Philippine Sea plate is converging at a rate of ~82 mm/yr with respect to the stable Eurasian plate, oblique to Taiwan's eastern coastline (Figure 3.1). Geodetic shortening rates slow progressively to the northwest (Yu et al., 1997) as Philippine Sea plate motion is transferred to north-south-trending thrust faults beneath Taiwan, and the oblique reverse Longitudinal Valley fault bounding the western margin of Taiwan's Coastal Range (Figure 3.1). Oblique convergence of the Philippine Sea plate in the Taiwan region results in a 94 mm/yr north to south migration of the suture zone (Suppe, 1984).

Migration of the suture zone results in incipient collision in the south, full collision in central Taiwan, and orogenic collapse in northern Taiwan (Figure 3.1; Shyu et al., 2005b; Suppe, 1984). The northeast-trending Longitudinal Valley is a 150- km-long valley bounding the eastern margin of Taiwan's Central Range (Figure 3.2). Valley width ranges between 0.8 and 7 km and averages 3 to 4 km, reaching a maximum altitude of over 300 m near Chihshang (Figure 3.2), where a major drainage divide occurs. The Longitudinal Valley fault accommodates oblique convergence between the Eurasian and Philippine Sea plates; accounting for about 32% of plate-normal shortening and 80% of the plate-parallel motion of the total Philippine Sea-Eurasian plate convergence (Angelier et al., 2000). Evolution of the arc-continent suture zone likely began 2 Ma or less (Barrier and Angelier, 1986). As Philippine Sea plate motion progressed northwestward, impingement of the Luzon Arc on the Eurasian continental sliver began to form contractional structures, exhuming the accreted rocks of the Luzon Arc-Trough system (Figure 3.1). Because of the southward propagation of the suture zone, the structures currently located southeast of Taiwan are early analogs to the more well-developed collisional structures northern Longitudinal Valley (Lundberg, et al., 1997). Two primary structures presently accommodate oblique shortening along the suture zone, they are the northwest-vergent, east-dipping Longitudinal Valley fault (LVF) and the east-vergent, west-dipping Central Range fault (CRF). As described below, both faults were involved in the September 2022 earthquake sequence.

The evolution of the Longitudinal Valley fault arc-continent suture zone is well documented by the volcanic, volcaniclastic, and sedimentary rocks of the Coastal Range orogen. The Miocene to early Pliocene Tuluanshan Formation forms the backbone of the Coastal Range and is composed of intermediate igneous and volcaniclastic rocks of the accreted Luzon Arc. Teng et al. (1988) describe the Tuluanshan Formation as an assemblage of mainly andesitic lavas and breccias (up to 1000 m thick), with lesser volumes of tuff, intrusive rocks, volcaniclastic rocks, and volcaniclastic rich limestone. (Kangkou Limestone) (Teng et al., 1988). Stratigraphically higher, the Fanshuliao Formation (also known as the Takangkou Formation) consisting of periodic mudstone/sandstone turbidites and mudstones, represents the first major pulse of continental and arc-derived sediment draped over the Tuluanshan Formation as the Luzon Arc was approaching Taiwan's eastern coast. Fanshuliao rocks are likely related to the fore-arc basin based upon the dramatic decrease in stratigraphic thickness from west to east across the arc (Chen and Wang,

1988). The Lichi Mélange, Miocene to Pliocene in age based on fossil assemblages (Chen and Wang, 1988) is a highly sheared mudstone found along most of the western margin of the southern Coastal Range (Figure 3.2). The chaotic mudstones of the Lichi Mélange are pervasively sheared and foliated, and contain exotic blocks of ophiolite, sandstone, and Tuluanshan-derived andesite, meters to kilometers in size (Page and Suppe, 1981). Key in understanding the nature of faulting along the Chihshang segment of the Longitudinal Valley fault (Figure 3.2) is the apparent effect Lichi Mélange rocks have on reducing the coupling strength of the fault zone. The Lichi Mélange is highly sheared and poorly indurated in most locales, especially in the Fuli-Chihshang region, and facilitates creep of the upper few kilometers of the Longitudinal Valley fault (e.g., Lee et al., 2001)

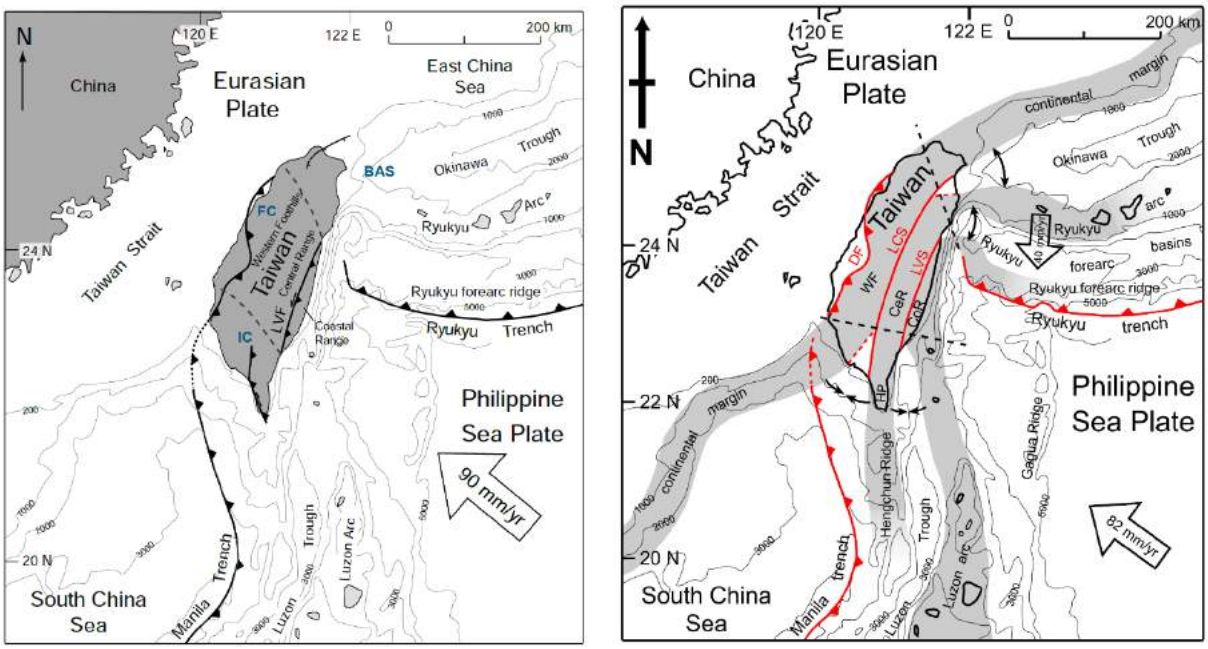

(a) (b)

Figure 3.1 Tectonic map of Taiwan (a) modified and (b) directly from Shyu et al. (2005).

3.1.1 Structure, Segmentation, and Slip History of the Longitudinal Valley Fault

Using conventional and GPS geodesy (Yu et al., 1997; Yu and Kuo, 2001; Angelier et al., 1997, 2000; Lee et al., 2001, 2006), rupture history (Shyu et al, 2007) and focal mechanisms (Kuochen et al., 2004), the Longitudinal Valley fault can be divided into several tectonic domains, delineated by the unique style of faulting at each locale. Along strike from north to south, both the nature and rate of fault slip vary considerably as a result of differing structural styles, fault orientations, and lithologies (Figure 3.2). In October and November 1951, numerous fault segments within the northern, central, and southern regimes of the Longitudinal Valley fault (Figure 3.2) ruptured, resulting in over 80 deaths and damage to thousands of buildings within the valley (Cheng, 1960; Hsu, 1971). The Mw 7.1 October 22 rupture occurred on the Meilun fault north of the city of Hualien (Hsu, 1971) (Figure 3.2); surface rupture may have propagated into the city itself (Bonilla, 1975). The November 25, 1951, surface rupture involved two separate events 3 minutes apart. The main shock occurred west of the town of Chihshang. Surface rupture occurred along the eastern margin of the Longitudinal Valley, north to the vicinity of Yuli (Figure 3.2). Rupture along

the Yuli fault and the Rueisuei–Kuangfu segment of the Longitudinal Valley fault produced the second shock three minutes later (Figure 3.2; Hsu, 1962; Shyu et al., 2007). Although rupture of the two segments is reported as contemporaneous, the Yuli and Longitudinal Valley fault segments are structurally distinct based on their style of rupture and show little or no overlap along strike (Figure 3.2). The northern tectonic domain of the Longitudinal Valley fault extends from the city of Hualien in the north to a region between the villages of Kuangfu and Rueisuei Figure 3.2; Shyu et al., 2005). The northern domain is characterized by obliquely convergent left-lateral strike-slip faulting. Recent GPS studies by Yu et al. (1997) and Yu and Kuo (2001) show a significant decrease in short-term shortening rates of the northern coastal range block, as well as decreased slip rates along the northern Longitudinal Valley fault. GPS-derived shortening azimuths of the northern Coastal Range (Yu et al., 1997; Yu and Kuo 2001) shift toward the north with respect to shortening azimuths further south, produced by a dominance of sinistral motion along the Longitudinal Valley fault. Northeast-striking reverse faults (Wang and Chen, 1993) accommodate northeast-directed strain within the northern Coastal Range (Yu and Kuo, 2001). Evidence for the dominance of strike-slip motion in the northern domain comes from the October 1951 earthquake where sinistral offsets of 2 m were accompanied by uplift of about 1.2 m. The central domain of the Longitudinal Valley fault extends from the Rueisuei– Kuangfu transition zone in the north, to Yuli in the south (Figure 3.2), where creep rates of the Longitudinal Valley fault begin to increase (Hsu and Bürgmann, 2006).

During the 1951 earthquake, the Yuli fault likely ruptured from the town of Yuli, north about 20 km, to a preexisting pop-up structure 4 km south of Rueisuei (Shyu et al., 2007) (Figure 3.2). During the November 1951 surface rupture, the main strand of the Longitudinal Valley fault did not rupture along the Yuli–Hsiukuluan canyon section, except along the 1.5 km overlap of the Yuli and Chihshang faults at the town of Yuli (Figure 3.2). The northern ~15 km of the central domain (Rueisuei segment) is characterized by well-defined reverse fault scarps several meters high in places. The Rueisuei segment enters the Coastal Range near Tzu-Chiang Prison approximately 5 km southwest of Kuangfu (Figure 3.2).

During the November 1951 earthquake, vertical displacement along the Rueisuei segment was typically greater than 1 m and more than 2 m locally (Shyu et al., 2007). The southern domain of the Longitudinal Valley fault, which includes the well-studied Chihshang segment, extends from Yuli to several kilometers south of the town of Luyeh (Figure 3.2). The Chihshang segment displays high rates of sinistral reverse creep facilitated in part by the Lichi Mélange (e.g., Yu and Liu, 1989; Angelier et al., 1997, 2000; Yu and Kuo, 2001; Lee et al., 2001, 2003; Hsu and Bürgmann, 2006), but also exhibits coseismic rupture (Hsu, 1962; Lee et al., 2006). The Chihshang segment is characterized by a listric geometry, steeply dipping 50° to 60° E in the upper ~17 km, shallowing to ~45° at depth (Kuochen et al., 2004; Lee et al., 2006; Wu et al., 2006). Creep rates on the main trace of the Chihshang segment are typically on the order of 15 to 22 mm/yr (Angelier et al., 1997, 2000; Lee and Angelier, 1993; Lee et al., 2001, 2003). Variations in creep rates come from spatial differences of geodetic surveys and different types of measurement apparatus as well as temporal variability related to the seismic cycle. Natural outcrops of the Chihshang fault are sparse and little is known about fault dip in the aseismic upper few kilometers. During the November 1951 earthquake sequence, rupture occurred first on the Chihshang segment with vertical coseismic displacements typically less than 0.5 m (Bonilla, 1975; Chung, 2003; Shyu et al., 2007).

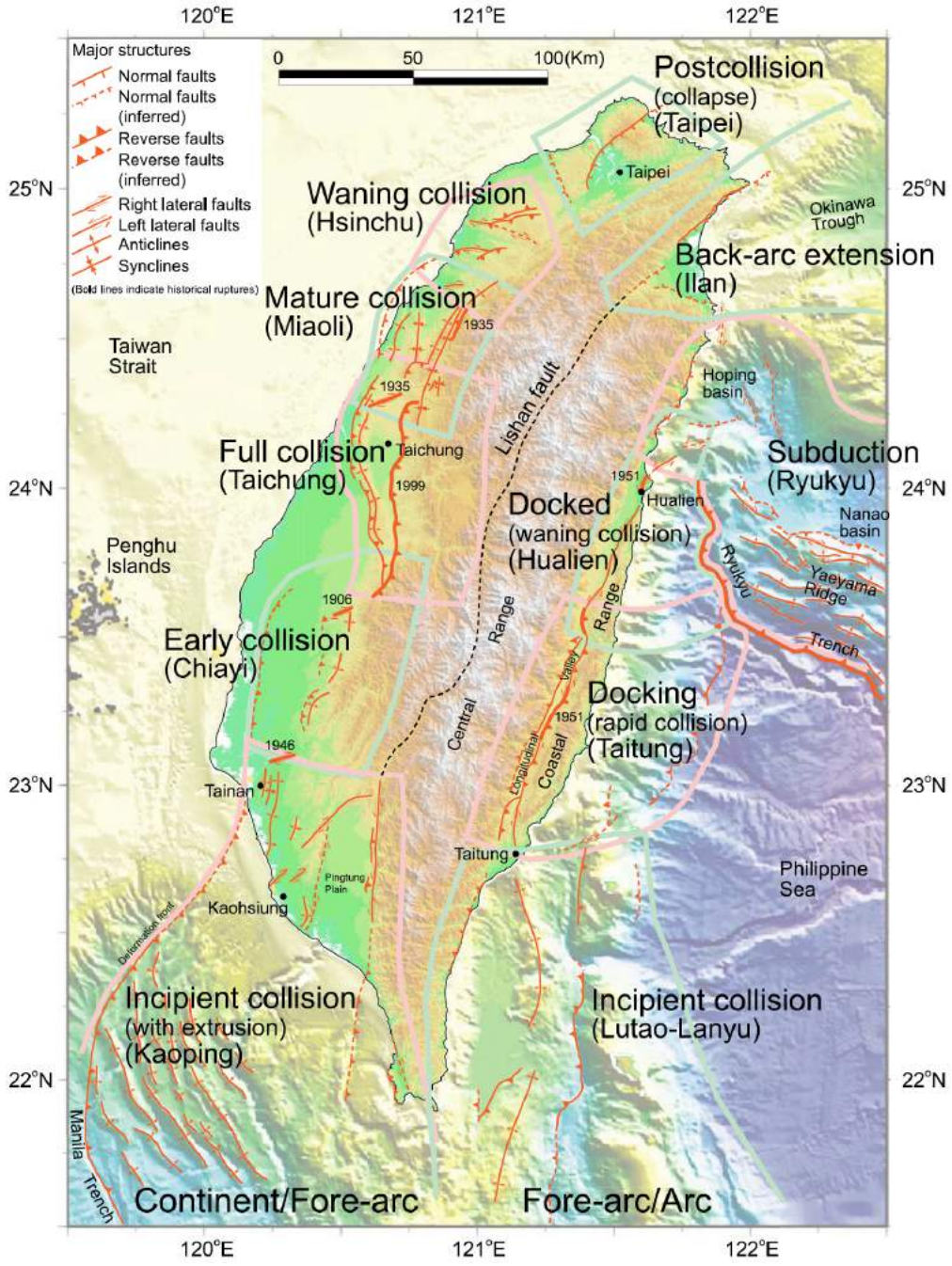

Figure 3.2 Taiwan fault structures, from Shyu et al. (2005).

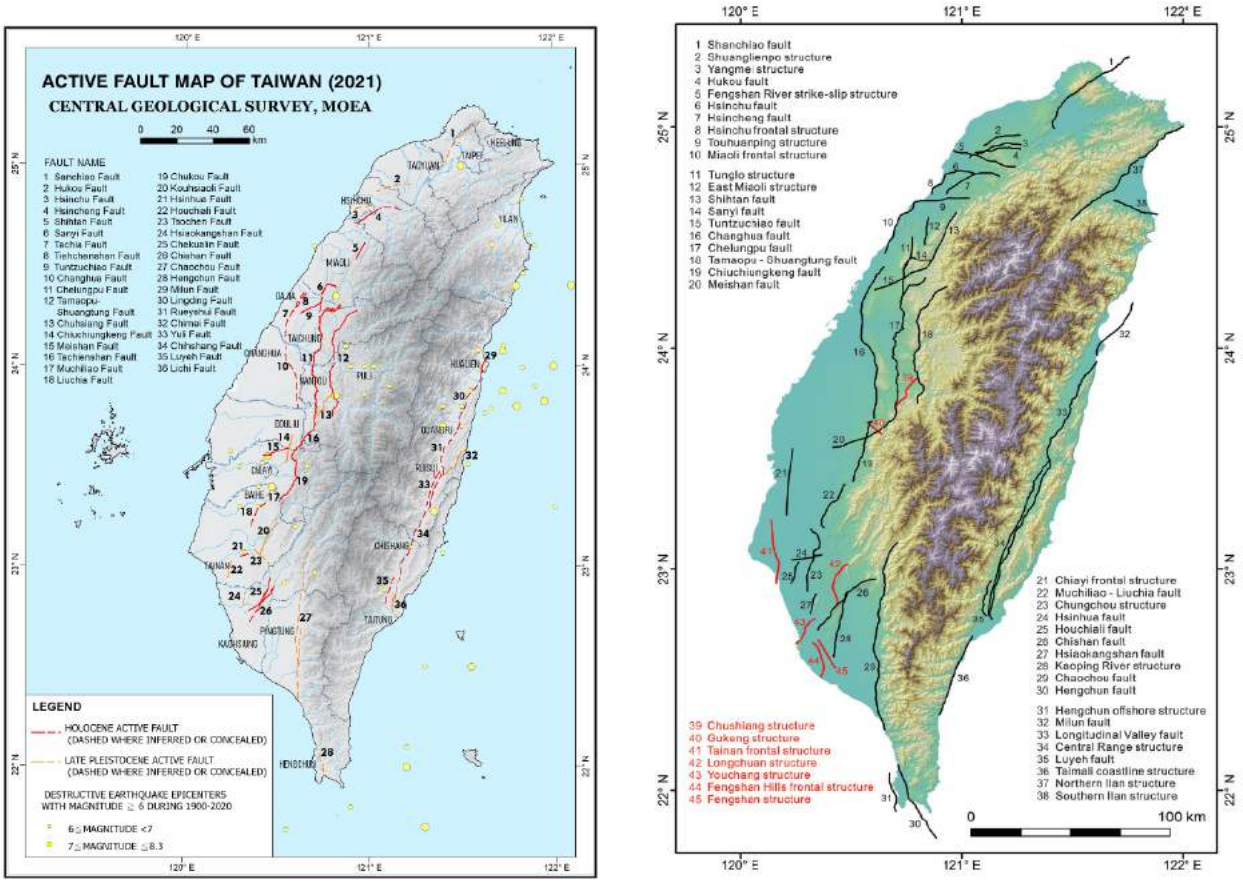

Figure 3.3 Active fault maps of Taiwan.

3.1.2 *Present-Day Uplift and Horizontal Shortening Rates of the Chihshang Segment of the Longitudinal Valley Fault*

Documentation of present-day horizontal shortening and uplift rates of the Longitudinal Valley began in the early 1980's with the installation of Academia Sinica's Taiwan GPS network and other conventional geodetic networks located throughout the Longitudinal Valley. As time progressed, more GPS stations, geodetic networks, leveling lines, and creep-monitoring instruments were surveyed, resulting in what is now a relatively clear picture of the present-day horizontal shortening characteristics of the Longitudinal Valley arc-continent suture zone. Horizontal shortening across the suture zone typically increases further to the south, ranging from 7 to 35 mm/yr with maximums commonly observed in the Fuli–Chihshang region. Uplift rates generally increase toward the south, reaching maximums near the Fuli/Chihshang region. Fault motion on Chihshang segment of the Longitudinal Valley fault is probably better constrained than at any other location along the Longitudinal Valley. Likely because of its well-known creeping behavior and rapid shortening, the Chihshang region has been host to a wide array of studies employing leveling (Yu and Liu, 1989), trilateration networks (e.g. Yu et al., 1990; Angelier et al., 1997), GPS arrays (Yu et al., 1997; Yu and Kuo, 2001), creepmeters (Lee et al., 2001, 2003), and infrared synthetic aperture radar (InSAR) monitoring (Hsu and Bürgmann, 2006). These studies suggest: (1) GPS-based horizontal shortening rates (spanning up to tens of kilometers) across

the LVF, not including the Central Range, are consistently in the range of 29–33 (Yu et al., 1997; Yu and Kuo 2001); (2) conventional geodetic network-based horizontal shortening rates measuring deformation on the scale of hundreds of meters to a few kilometers, are typically 20–22 mm/yr, 10 mm/yr lower than GPS-derived rates crossing similar fault locations (Angelier et al., 1997; Angelier et al., 2000); (3) Coastal Range uplift rates in the Fuli/Chihshang region range from 13–21 mm/yr (Yu and Liu, 1989; Angelier et al., 2000, Hsu and Bürgmann, 2006); and (4) the majority of fault-related deformation is confined to a relatively narrow zone, as narrow as 20 m at Chihshang and up to 120 m wide near Fuli (Yu and Liu, 1989), although InSAR monitoring suggests creep may produce minor deformation several hundred meters from the fault (Hsu and Bürgmann, 2006).

3.2 Summary of the CRF

In contrast to the LVF, the CRF fault has received comparatively limited attention regarding its role in accommodating oblique collision in southeast Taiwan. As noted by Shyu et al. (2006a), there was debate as recently as the early 2000's about whether the CRF was a normal or reverse fault. Despite the prominent expression of the rangefront, regional uplift rates on the order of 3-6 mm (Dadson et al., 2003), and abundant uplifted lateritic terrace and alluvial fan surfaces (Shyu et al., 2006a), evidence of throughgoing fault daylighting along the rangefront margin is limited. Work by Shyu et al. (2006a) documented geomorphic features along the fault from the Chihshang area to Rueisuei and determined the uplift rate was ~6.4 mm/yr, but on uplift of the actively folding Wuhe tableland. Notably the strike of the tableland fold axis is rotated approximately 25° clockwise from the strike of the fault parallel to the rangefront to the south, suggesting the fold could be a response to an orientation more favorable to shortening. The rangefront along the CRF generally lacks the obvious scarps offsetting terrace and fan surfaces that are common along both the Chihshang and Rueisuei-Kuangfu sections of the LVF. Huang et al. (2010) estimated a slip rate for the CRF 10.1 to 14.1 mm/yr from geodetic models, Shyu et al. (2006) determined the slip rate was likely less than 12.8 mm/yr, and Shyu et al. (2020) utilized a rate of 4.8 to 11.2 mm/yr for the CRF structure as a whole. Although significant uncertainties exist regarding slip rate owing to a lack of exposures and strain gauges, it is clear that the fault accommodates strain at rates considerably lower than the LVF at rates of about 20 to 40 mm/yr (noted above).

In October 2013, an **M** 6.4 earthquake occurred north the town of Rueisuei, with an aftershock distribution occurring mostly beneath the valley axis for a distance of ~20 km (Lee et al., 2014). Work by Chuang et al. (2014) and Lee et al. (2014) indicates the event likely occurred on a moderate to steeply west-dipping fault that appears to intersect the LVF updip, several kilometers below the ground surface. Both the Chuang et al. (2014) and Lee et al. (2014) publications indicate rupture on a blind strand CRF that intersects LVF (Figure 3.6). This model bears similarities with the Shyu et al. (2006) model of the LVF where the opposing LVF and CRF may interact at depth. Chuang et al. (2014) indicate that the fault represents the blind margin of a Central Range backthrust or retrowedge, and that the 2013 Rueisuei earthquake together with the 2006 Taitung earthquake support the activity along the entire CRF.

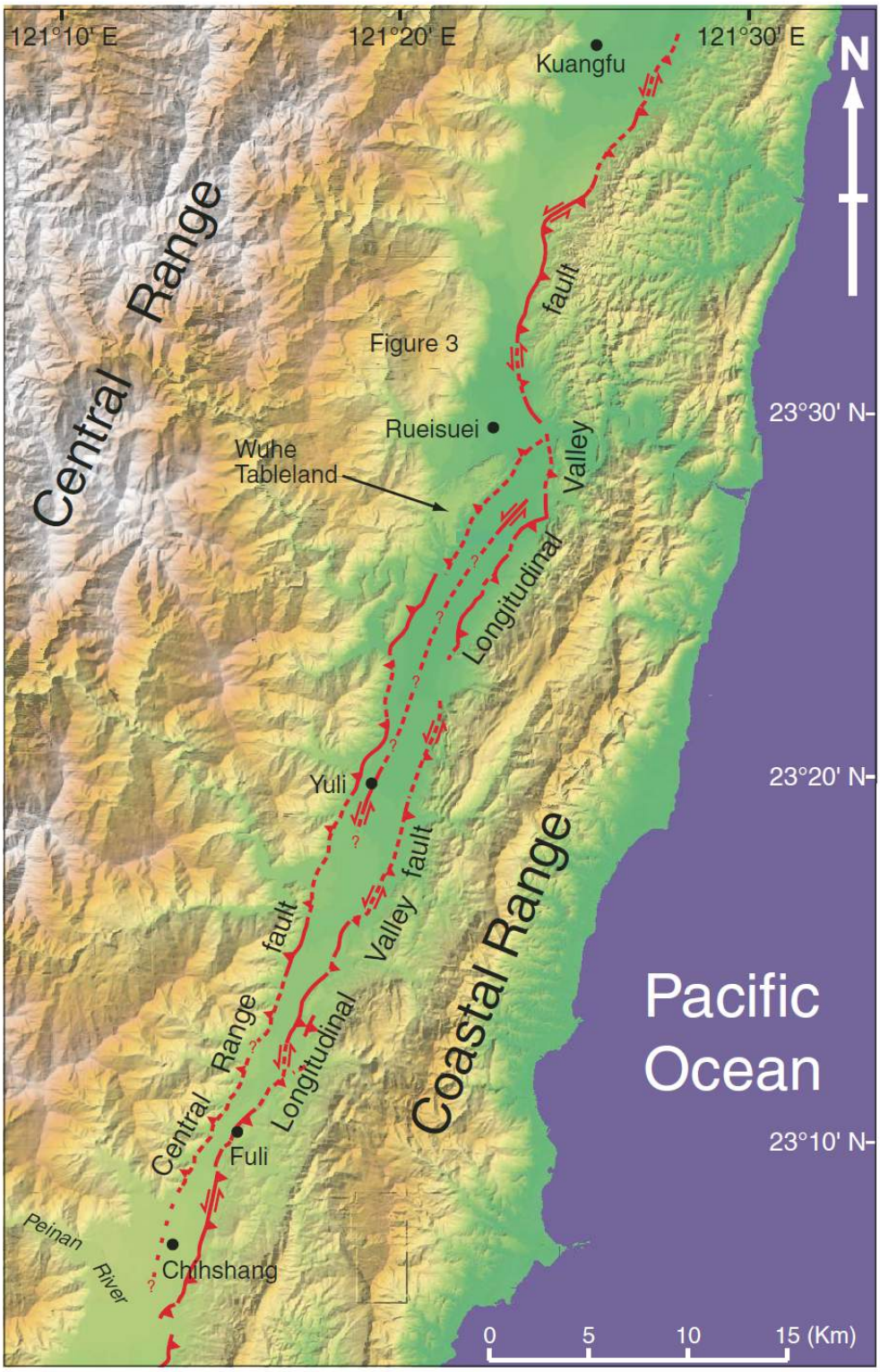

Figure 3.4 Tectonic map of Taiwan's Coastal Range (adapted from Shyu et al, 2006).

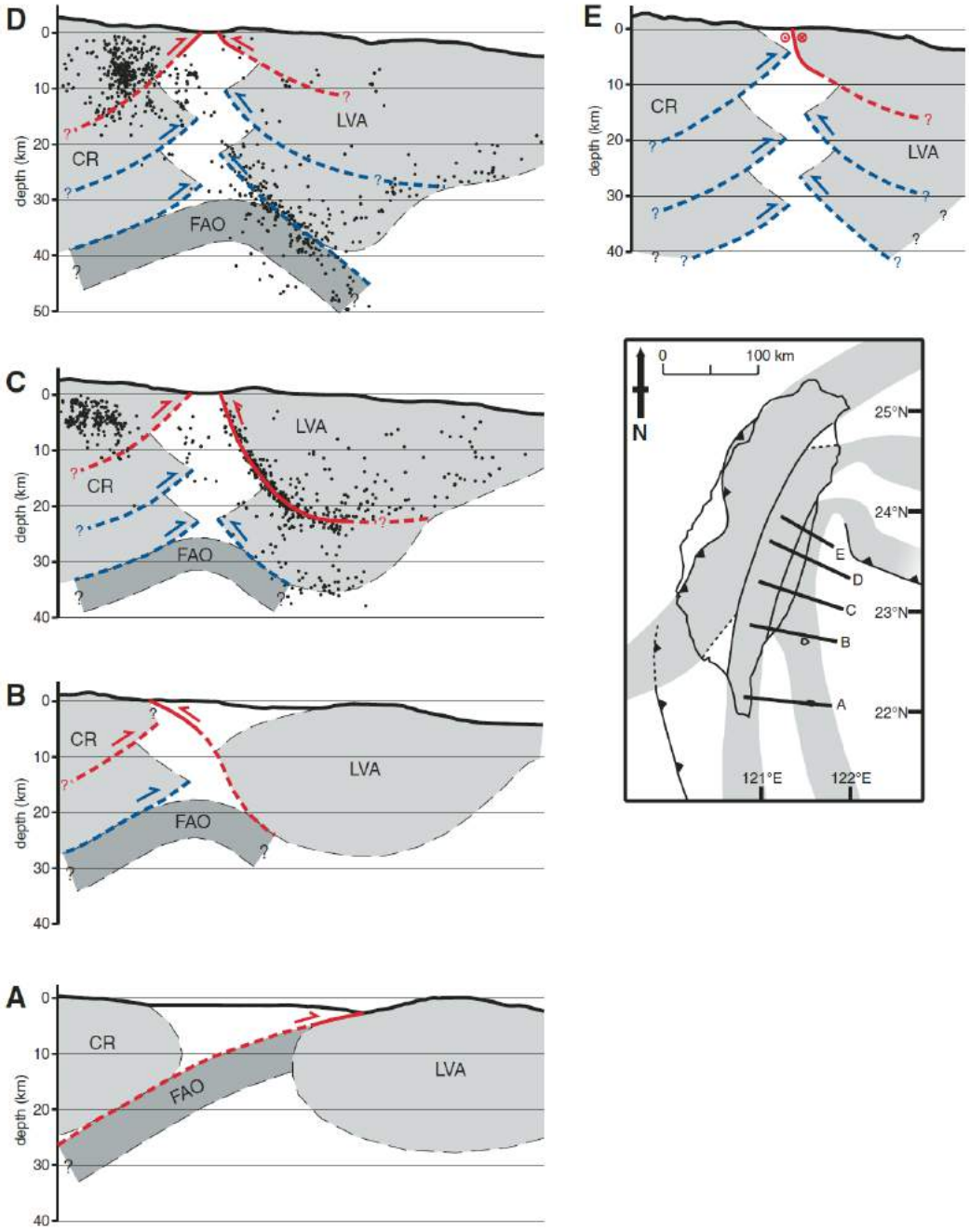

Figure 3.5 Schematic crustal cross-sections depicting the Shyu et al (2006) hypothesis of the ‘‘Christmas tree’’ model for the evolution of the Longitudinal Valley suture. Each section is drawn using current topography and observations along the lines specified on the index map, with no vertical exaggeration. Red indicates the youngest and currently active faults in each time frame, and blue indicates older faults, which may still be active. Faults are dashed where inferred Relocated earthquake hypocenters in Figures C and D are adapted from Kuochen et al. (2004)

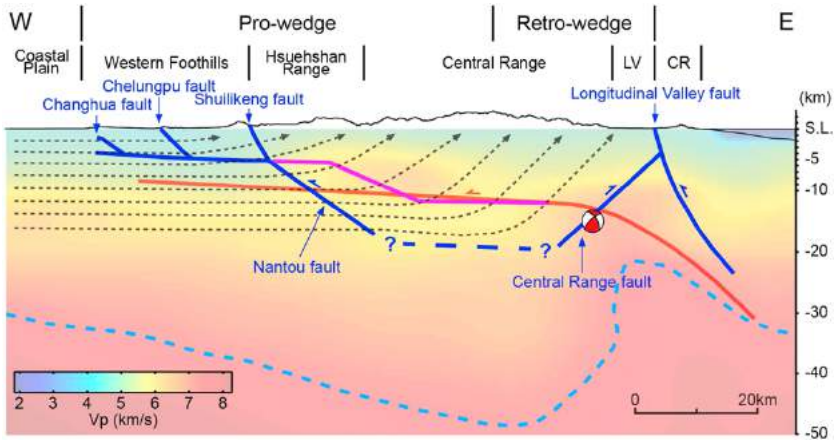

Figure 3.6 Cross section of Taiwan orogenic wedge from Chuang et al (2014). Blue lines are major faults after Chuang et al. (2013). Focal mechanism shows the Rueisuei earthquake. P wave velocity tomography image is from Kuo-Chen et al. (2012). Dashed blue line indicates iso-surface of 7.5 km/s P wave velocity. CR: Coastal Range; LV: Longitudinal Valley.

3.3 2022 Chishang earthquake sequence ground motions

The 2022 Chishang earthquake sequence occurred within the narrow and elongated Longitudinal Valley, approximately at the level of cross section C of Figure 3.5. The 2022 earthquake sequence hypocenters were located to the west of the Longitudinal Valley, with the mainshock close to the town of Chihshang (Figure 3.7). This event demonstrated that the CRF accommodates also present-day plate boundary shortening, and that the LVF and CRF together form an active head-to-head, conjugate fault system (Figure 3.7) (from Tang et al, 2023).

The consequence of the unique rupture mechanism from south to north manifested in strong evidence of forward directivity effects, with strong associated pulse-like velocity motions; as well as single-sided velocity pulses normal to the direction of rupture propagation that resulted from the accommodation of the tectonic slip of the complex normal-reverse rupture communication. Typical pulse like motions extracted by NAR Laboratories are shown in Figure 3.7 below for the **M**6.9 mainshock and the **M**6.5 foreshock.

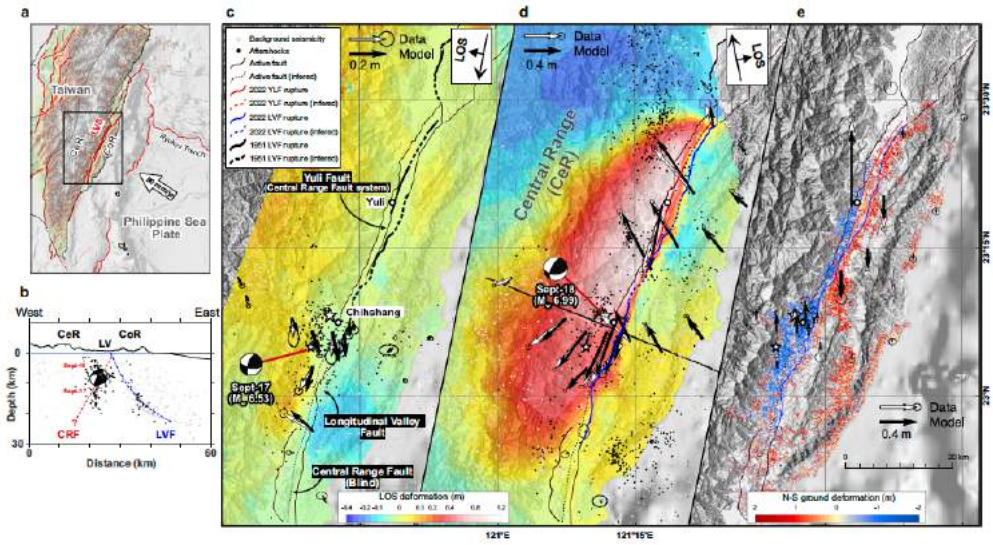

Figure 3.7 (from Tang et al, 2023) **a.** Tectonic setting of the Longitudinal Valley suture zone (LVS). CeR: Central Range; CoR: Coastal Range. **b** Cross section view showing the distribution of background seismicity between 1990 and 2020 (light gray dots). Relocated aftershocks prior to November 17 are in black dots (catalog from Taiwan Geophysical Database Management System, Taiwan GDMS). See (**d**) for profile location. **c** Coseismic interferogram and GNSS horizontal displacements for the foreshock. Traces of the Central Range fault and the Longitudinal Valley fault (LVF) are based on the Taiwan Earthquake Model. Traces of the 1951 surface ruptures on the Yuli fault (YLF) and the LVF are based on previous field surveys. LOS: radar line-of-sight direction. **d** Coseismic interferogram and GNSS horizontal displacements for the mainshock. **e** Cumulative N–S offsets from the foreshock to the mainshock. Vectors represent the GNSS vertical coseismic displacement for the mainshock.

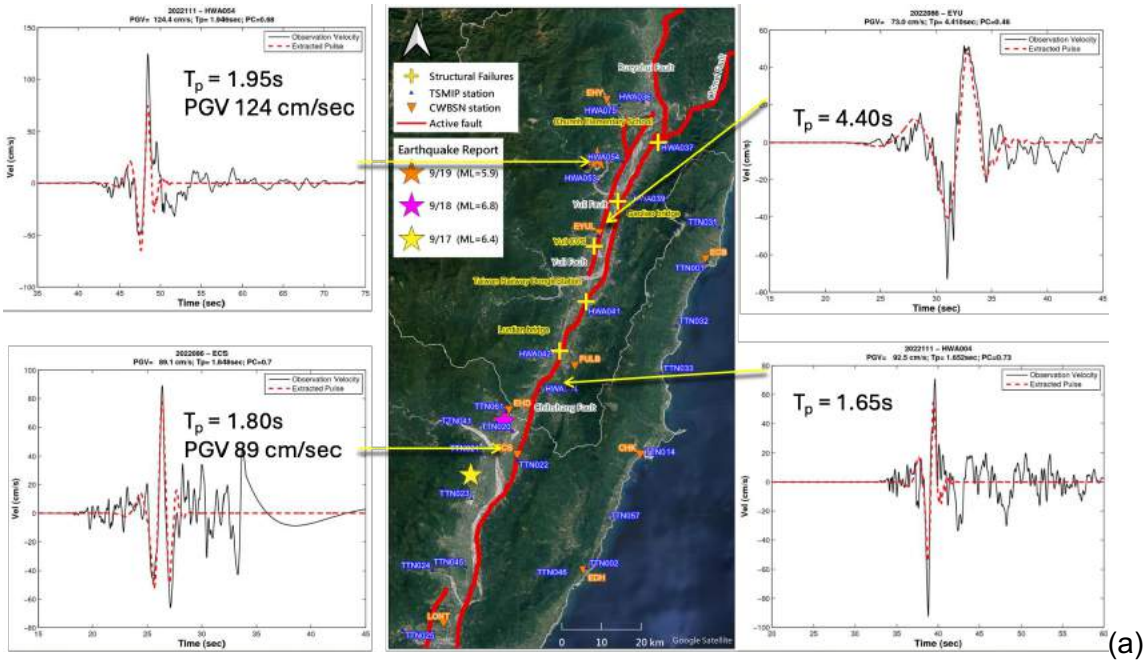

(a)

Figure 3.8 (cont)

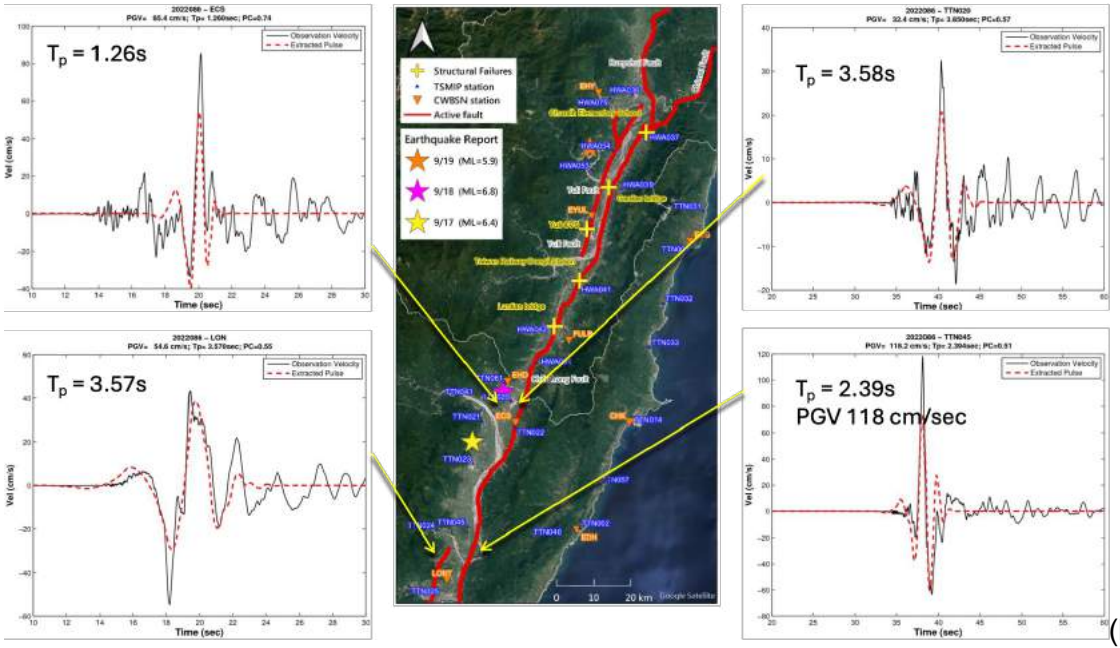

Figure 3.8. Pulse like motions extracted by NARLabs from the Chihshang mainshock (a) and the Guanshan foreshock (b); each ground motion time series depicts the extracted pulse-like motions, their period, and the peak ground velocity, where applicable.

The uniqueness of the ground motions of this event pertains to their proximity to the longitudinal fault structure: the ensemble of strong motion stations that got access to through our interaction with NCREE and the NARLabs, lied within 10km of the surface projection of the rupture plane. Figure 3.9 plots the magnitude-distance distribution of the Guanshan and the Chihshang events on the same distribution as the NGAWest2 database (Ancheta et al, 2014) where one can see that they lie in the sparsely populated zone of near-fault, large magnitude events.

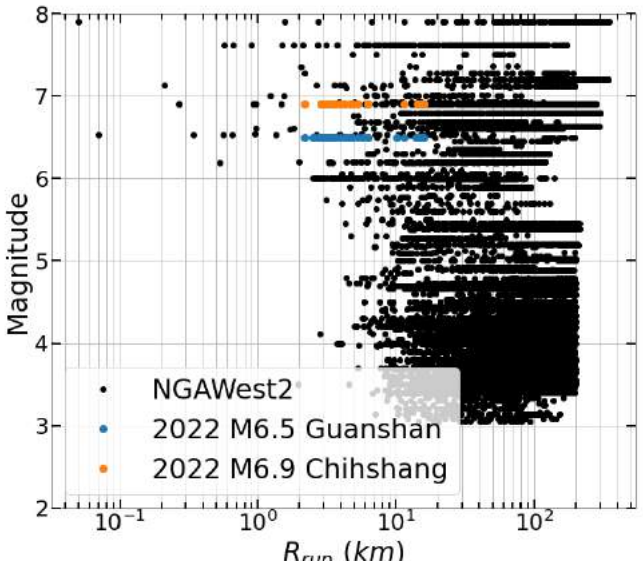

Figure 3.9 Distribution of magnitude-distance of the M6.5 Guanshan and M6.9 Chihshang events, plotted alongside the NGAWest2 database for reference.

To recover the tectonic offset from the ground motion time series, we used the instrument corrected ground motions and applied alternative baseline correction techniques including the Boore (1999) and Boore (2000) methodologies of quadratic and bilinear baseline correction correspondingly. A demonstration of each one of these methods is shown in Figure 3.10.

3.4 Tectonic offset: Ground motions vs. GPS measurements

A novel modification that we implemented in this work is that we imposed the constraint of t_q for the quadratic baseline correction (Figure 3.10a) and the times t_1 and t_2 for the bilinear correction (Figure 3.10b) to be common for all three components. Our hypothesis is that the instrument is tilting as a rigid body, and as a consequence, the three components cannot independently be affected by the instrument motion during the pre-event, strong shaking, and post-event period.

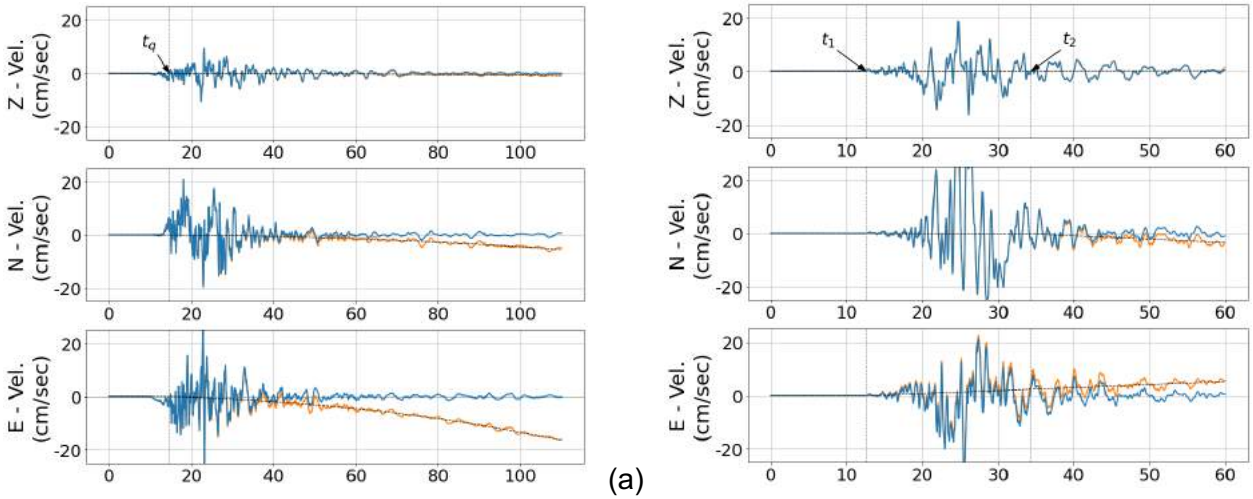

Figure 3.10 Instrument tilt correction simultaneously for all three components using the Boore (1999) quadratic baseline correction method (a) and the bilinear method (b).

Results shown below were then compared with GPS observations made by the network of more than 400 Global Navigation Satellite System (GNSS) stations operated by several institutes and universities continuously, and used to produce high-precision, three-component velocity fields as well as position time series that track time-varying crustal deformation across the entire Island of Taiwan. Results were found in excellent agreement, in the horizontal and vertical directions. More details on the methodology will be provided in a manuscript in progress. The location of the GPS stations and measured horizontal and vertical vectors are shown in Figure 3.11.

Results for the tectonic offset estimated by our method from the **M**6.9 Chihshang maishock are shown in Figure 3.12. As mentioned above, our slip estimates from the strong motion records are consistent with the GNSS (1Hz) GPS, with the largest offset observed in the middle and Northern end of rupture. On the Central Range Fault (CRF) hanging wall, we estimated specifically up to 1m left lateral slip and 1m uplift; while on the Longitudinal Valley Fault (LVF) hanging wall, we observed a range of shortening from approximately 90cm in the vicinity of the rupture to 30cm at a distance 14 km away, near the eastern coastline. By contrast, the largest tectonic offset of the **M**6.5 foreshock was observed near the southern end on the rupture, while the largest tectonic offset was on the order of 20 cm (Figure 3.13).

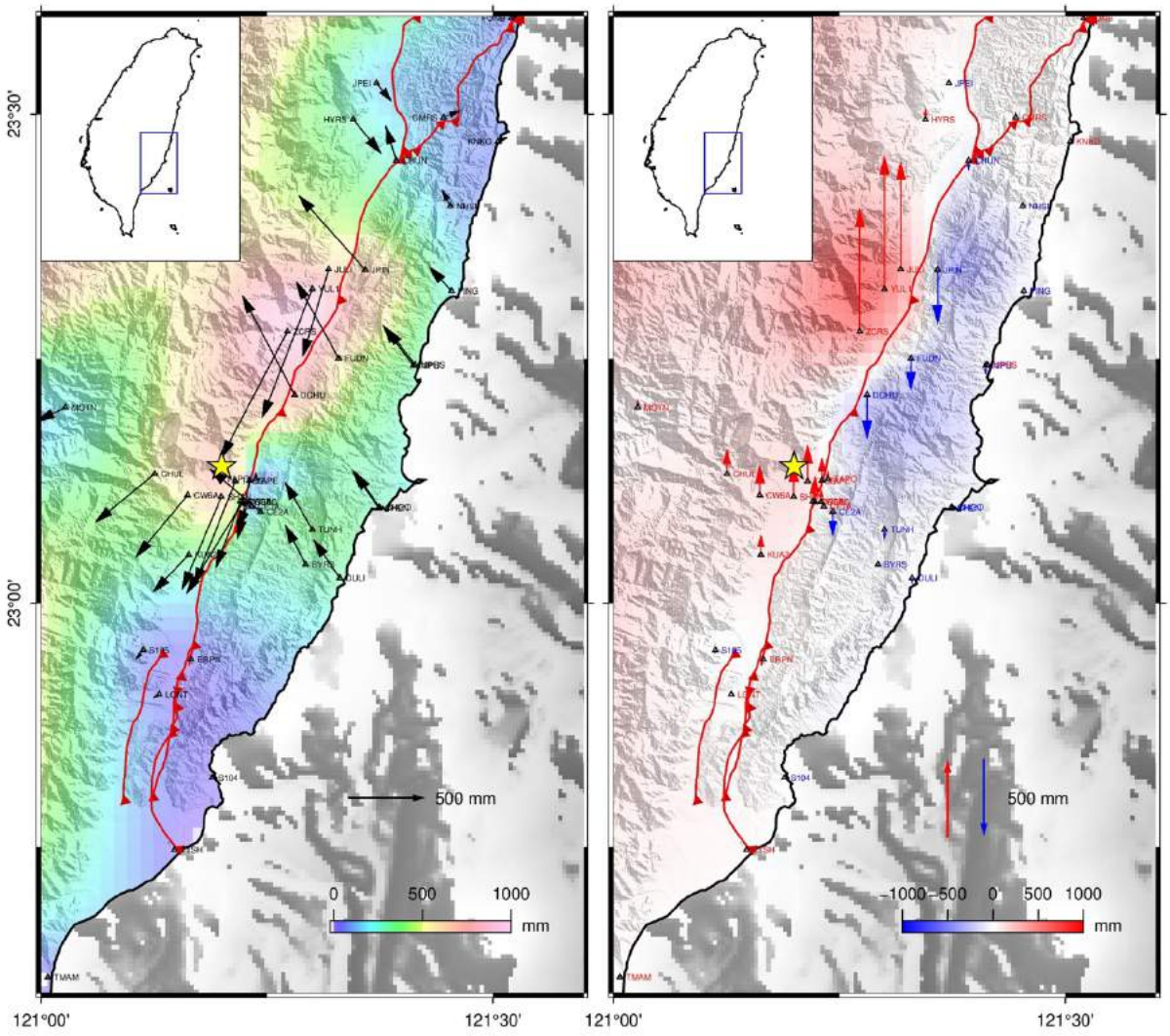

Figure 3.11 Horizontal and vertical permanent offset measured by the GNSS network in the vicinity of the M_w6.9 Chihshang earthquake epicenter. The maximum horizontal displacement was measured in the GPS station ZCRS south of Yuli town, with displacement of 1000 mm, while station DYES north of Yuli measured the largest uplift, 1100 mm (https://tgm.earth.sinica.edu.tw)

3.5 Peak-to-Peak Velocity Pulses

Focusing on the velocity pulses, which --as we will see in Chapter 5, were catastrophic for the integrity of the longitudinal valley bridges-- Figure 3.14 plots the vectors of peak-to-peak horizontal velocity pulses along the rupture. Two main conclusions can be drawn from this figure: the strong fault normal pulses in rupture direction are manifestations of forward directivity effects, are double sided and increase towards the north, while the strong fault parallel pulses accommodating permanent slip are single sided and have non-zero integral displacements.

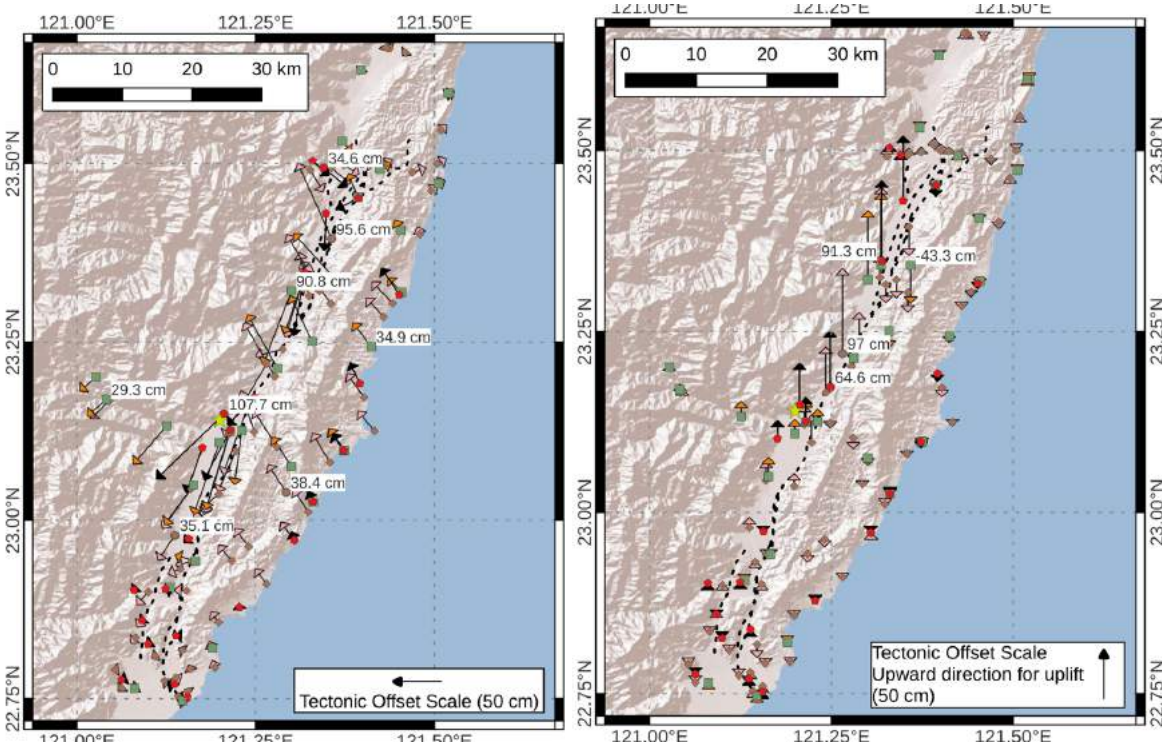

Figure 3.12 Comparison of tectonic offset estimated from the strong motion records by the GEER team (black arrows) and the GNSS stations (orange arrows). Recordings from the M_w6.9 Chihshang mainshock.

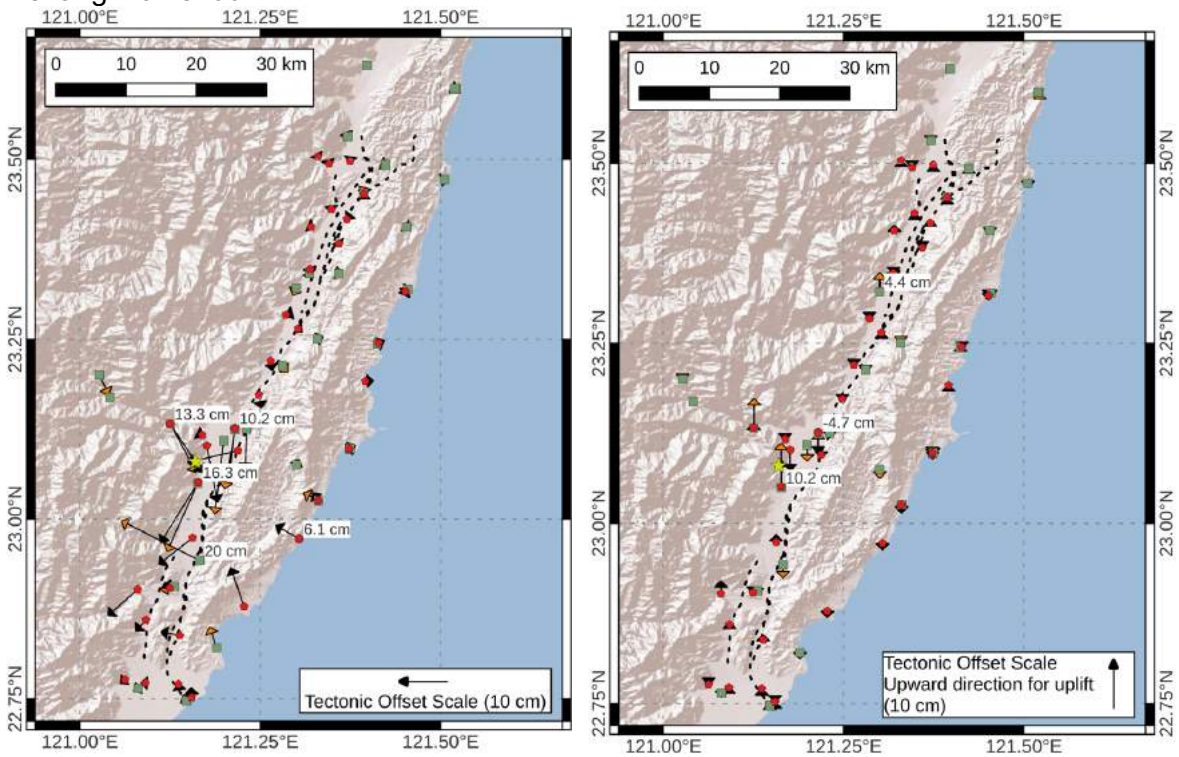

Figure 3.13 Comparison of tectonic offset estimated from the strong motion records by the GEER team (black arrows) and the GNSS high-rate GPS stations (orange arrows). Recordings from the M6.5 Guanshang mainshock.

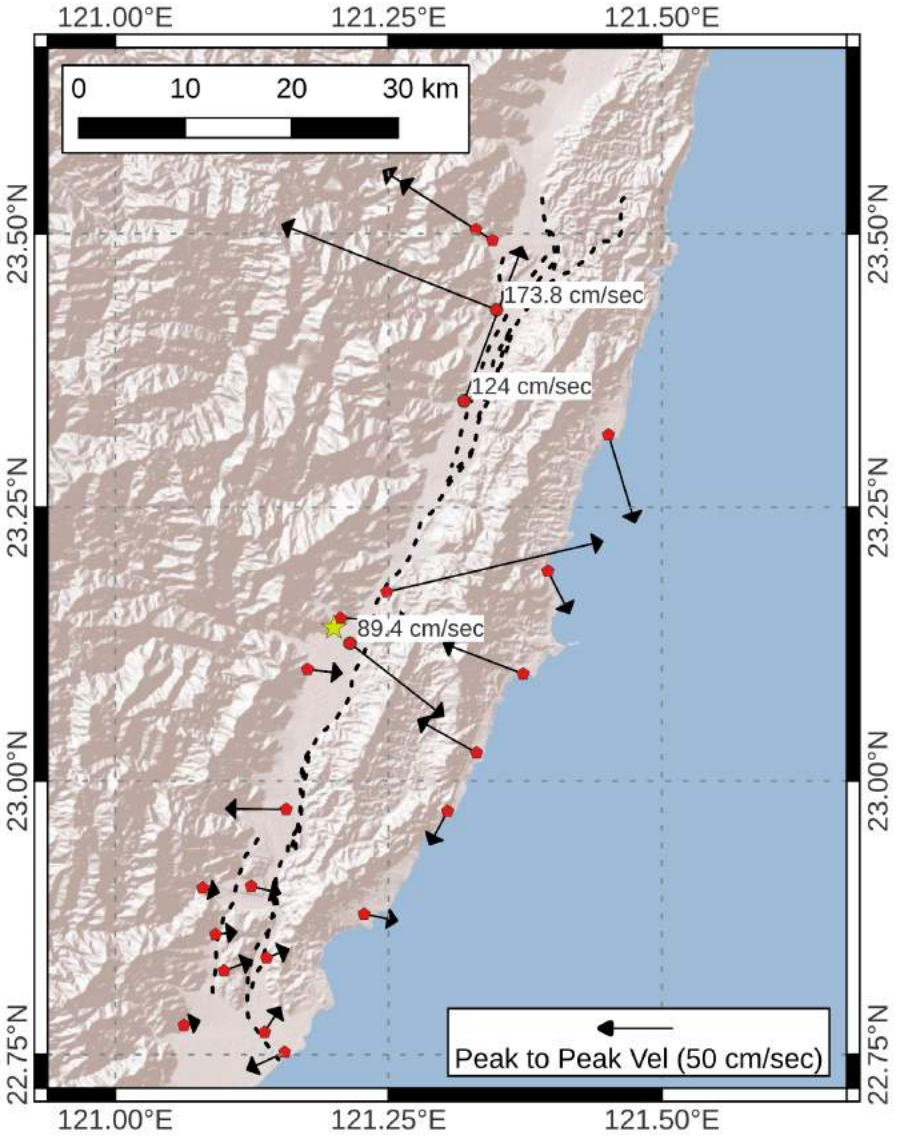

Figure 3.14 Peak-to-peak velocity vectors extracted from strong ground motion time series along the rupture (**M**6.9 Chihshang mainshock).

Examples of processed horizontal ground motion time series at stations that showed permanent tectonic offset are shown in Figure 3.15. Note that in Figure 3.15(a), the large double sided EW velocity pulse is a forward directivity pulse that integrates to zero tectonic offset but locally has a very large dislocation of approximately 80cm. The opposite is true (i.e. the lack of pulse like motions) for the strong motion records that integrate in permanent tectonic offset up to approximately 1m.

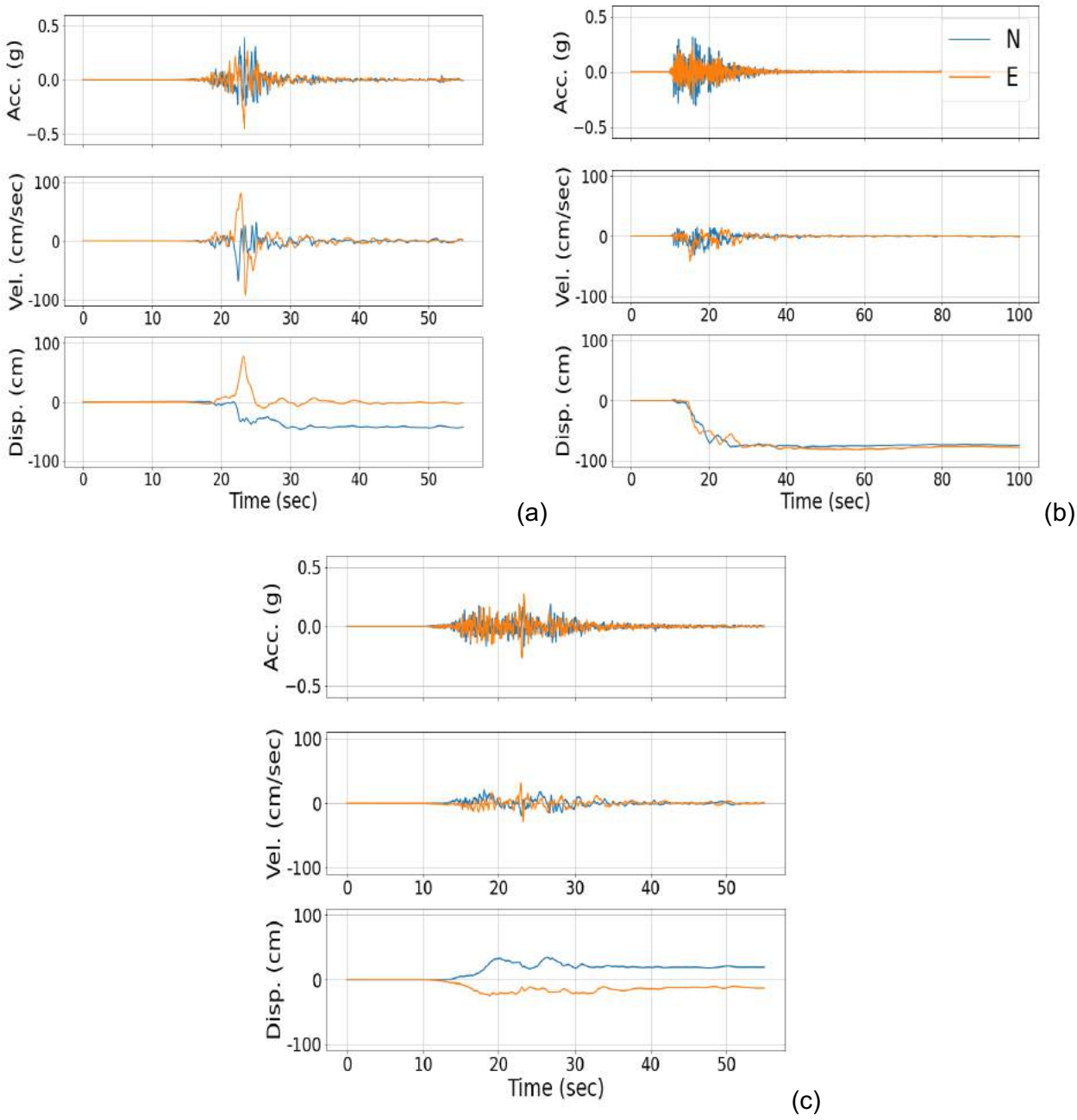

Figure 3.15 Examples of horizontal strong ground motions, processed by the modified Boore (1999, 2000) baseline correction to recover the tectonic offset. A second dataset that was not processed using the quadratic or bilinear baseline correction, was processed the NGA PEER processing protocols.

3.6 Comparison to Ground Motion Models

Lastly, we evaluated the scaling of the mainshock ground motions in Figure 3.16 for the tectonic environment in Taiwan and four of the widely used NGAW2 ground motion models. We observed below average short period motions; above average medium and long period motions; and GMM under-estimation of the significant duration, all of which could be consistent of very strong

nonlinearity in the area that overdamps the high frequencies, amplifies the long periods and elongates the reverberation of the latter in the longitudinal valley. Our GMM comparison was also shown to be very sensitive to the finite-fault geometry which at the time was estimated using kinematic source inversion methodologies.

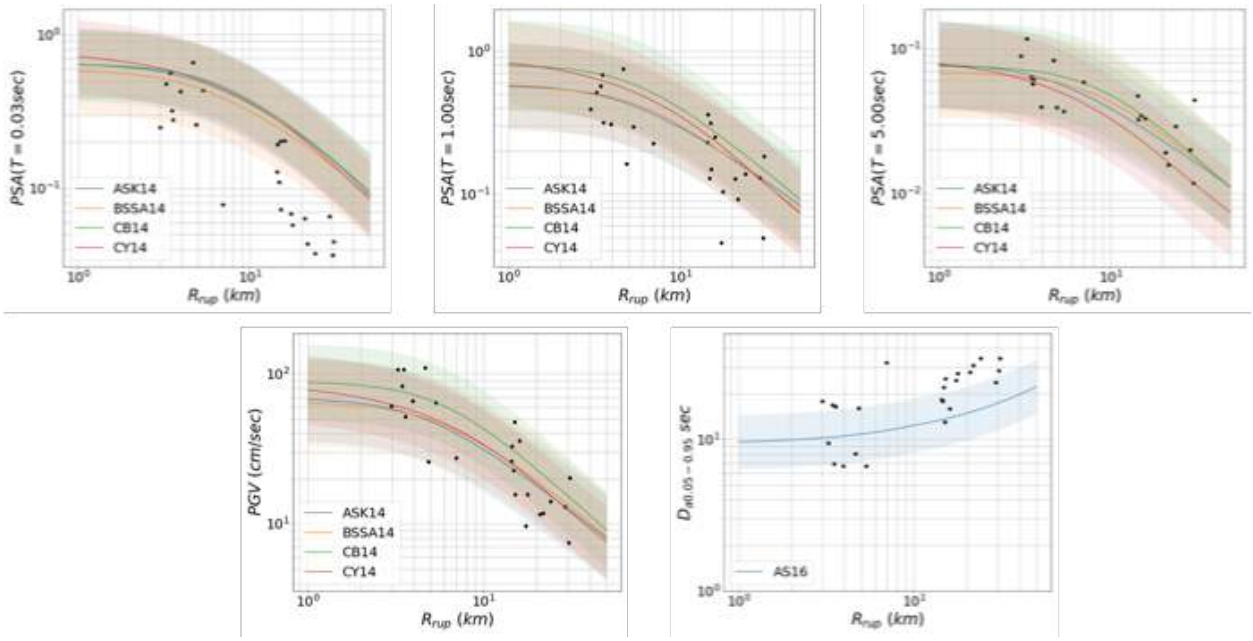

Figure 3.16 Ground motion scaling of the **M**6.9 Chihshang strong ground motions.

REFERENCES

Ancheta, T. D., Darragh, R. B., Stewart, J. P., Seyhan, E., Silva, W. J., Chiou, B. S. J., ... & Donahue, J. L. (2014). NGA-West2 database. *Earthquake Spectra*, *30*(3), 989-1005.

Angelier, J., Barrier, E., Chamot-Rooke, N., Lave, J., & Rangin, C. (2000). Seismic behavior of the Taiwan orogen: insights from a deep seismic reflection profile across the Longitudinal Valley. Tectonics, 19(1), 136-159.

Barrier, E., & Angelier, J. (1986). The Taiwan collision zone: A preliminary result of a geodetic study. Earth and Planetary Science Letters, 78(1-2), 7-20.

Chen, C. H., & Wang, K. L. (1988). The evolution of arc-continent collision in the Taiwan-Luzon region. Tectonophysics, 149(3-4), 211-230.

Ching, K. E., Ji, C., Wald, D. J., & Helmberger, D. V. (2004). Slip history of the 2003 Mw 6.5 Chengkung, Taiwan, earthquake from joint inversion of teleseismic, GPS, and strong-motion data. Bulletin of the Seismological Society of America, 94(6B), S218-S228.

Chuang, R. Y., Hsu, Y. J., Liu, C. S., & Lin, Y. N. (2014). Rupture process of the 2013 Rueisuei, Taiwan, earthquake inferred from strong motion data. Geophysical Research Letters, 41(7), 2234-2241.

Hsu, S. K., & Bürgmann, R. (2006). Creep along the Central Longitudinal Valley Fault from 1 year of continuous GPS data. Geophysical Research Letters, 33(21).

Huang, C. Y., Zhao, W., Wu, C. C., Sun, Y., & Dong, J. J. (2010). Three-dimensional slip distribution of the 1999 Chi-Chi, Taiwan, earthquake from inversion of GPS data. Bulletin of the Seismological Society of America, 100(1), 341-354.

Kuo-Chen, H., Wu, Y. M., Chang, C. H., Hu, J. C., & Chen, W. S. (2004). Relocation of Eastern Taiwan Earthquakes and Tectonic Implications, *Terrestrial* 4.

Kuo-Chen, H., F. T. Wu, and S. W. Roecker (2012), Three-dimensional P velocity structures of the lithosphere beneath Taiwan from the analysis of TAIGER and related seismic data sets, J. Geophys. Res., 117, B06306, doi:10.1029/2011JB009108.

Lee, J. C., Angelier, J., Chang, T. Y., Lee, C. T., Tu, Y. F., Chueh, H. T., ... & Chang, Y. L. (2001). Active deformation of Taiwan from GPS measurements and tectonic implications. Tectonophysics, 335(1-2), 15-39.

Lee, J. C., & Angelier, J. (1993). The mechanism of active deformation of Taiwan: A synthesis from the observations across the western foothills. Tectonophysics, 217(1-4), 57-73.

Lee, J. C., Sieh, K., Chen, Y. G., Liu, T. K., Mueller, K., & Chen, C. C. (2006). A semi-preemptive earthquake forecasting experiment in Taiwan, July 2002–June 2003. Geophysical Journal International, 165(2), 493-516.

Page, B. M., & Suppe, J. (1981). The Pliocene Lichi melange of Taiwan; its plate-tectonic and olistostromal origin. *American Journal of Science*, *281*(3), 193-227.

Shyu, J. B. H., Chung, L. H., Chen, Y. G., Lee, J. C., & Sieh, K. (2007). Re-evaluation of the surface ruptures of the November 1951 earthquake series in eastern Taiwan, and its neotectonic implications. *Journal of Asian Earth Sciences*, *31*(3), 317-331.

Shyu, J. B. H., Sieh, K., Chen, Y. G., Lo, C. H., Lin, C. T., & Mueller, K. (2006). Neotectonics of the Longitudinal Valley fault: distributed deformation across faults and folds. Geological Society, London, Special Publications, 247(1), 171-192.

Shyu, J. B. H., K. Sieh, and Y.-G. Chen (2005), Tandem suturing anddisarticulation of the Taiwan orogen revealed by its neotectonic elements, Earth Planet. Sci. Lett.,233, 167–177.

Suppe, J. (1984). Mechanics of mountain building and metamorphism in Taiwan. Memoir - Geological Society of America, 158, 1-37.

Teng, L. S., Hsieh, Y. L., & Chung, S. L. (1988). The arc-continent collision in Taiwan. Tectonophysics, 149(3-4), 281-305.

Yu, S. B., Hwang, C., & Kuo, L. C. (1997). Three-dimensional crustal deformation determined by GPS measurements in the Taiwan area. Journal of Geophysical Research: Solid Earth, 102(B8), 17801-17815.

Yu, S. B., & Kuo, L. C. (2001). Three-dimensional crustal velocity field of the Taiwan area obtained from the analysis of continuous GPS observations. Geophysical Journal International, 144(3), 485-496.

4. OBSERVATIONS OF SURFACE RUPTURE

Documenting the distribution and related effects of surface fault rupture associated with the September 17th and 18th earthquakes was a primary task of the GEER team's reconnaissance effort. The surface rupture team lead was Brian Gray.

Prior to the start of field reconnaissance on October 18th, it was understood that geologists from Taiwan's Central Geological Survey and researchers from multiple Taiwanese academic institutions had been in the field documenting surface rupture in the weeks following the earthquakes. To avoid duplicating the ongoing Taiwanese efforts where possible, the surface rupture team worked to document surface rupture with a focus on engineering-related topics including: 1) surface rupture/structure interaction, 2) distribution and rupture zone width, 3) triggered/off-fault deformation, 4) oblique strain accommodation, and 5) expression of surface faulting at sites with prior historic ruptures.

1. To provide context for damage observations, the team was interested in documenting fault/structure interaction and related structure performance. Although the ~40-km-long surface rupture occurred primarily in rural farming areas, much of the rupture interacted with the built environment, crossing numerous roads, retaining walls, water conveyances (mostly concreted-lined canals), rural housing developments, school grounds, bridges and approach structures, and Taiwan's southeastern rail line. A key challenge of documenting surface rupture in the built environment was distinguishing long-term creep-related deformation from coseismic slip and afterslip.
2. The Chihshang segment of the LVF represents a plate boundary structure that accommodates large components of shortening and left-lateral translation. As it relates to the design of engineered structures, the team was interested in understanding how these slip components were manifest as surface rupture.
3. Repeated historic surface rupture expression. The LVF has experienced multiple surface rupture events in the last 75 years including the 1951 Longitudinal Valley earthquake sequence, the 2003 Chengkung earthquake, the March 23, 2022 **M**6.7, and the **M**6.5 and **M**6.9 earthquakes of September 2022. The team was interested in understanding how these events were expressed as surface rupture over the course of multiple events.
4. Understanding the potential for triggered displacement (triggered slip on a fault or fault zone that did no not generate the causative earthquake) remains a poorly understood element of fault displacement studies for engineered structures. Given the initial reports of triggered slip on the LVF, the surface rupture team was interested in learning whether other nearby faults (e.g., Yungfong and Tuluanshan) in the coast range accommodated additional triggered displacement.

From a larger perspective, the team was interested in collecting data to better understand the distribution of surface rupture relative to the CRF (causative) and LVF (ancillary) structures. Initial seismological observations indicated the LVF was apparently not responsible for the primary (September 18th) event based on the steep southwest dip of the interpreted nodal plane coincident with aftershock distribution. However, field reports suggested that much of the surface rupture near the latitude of the epicenter was located along the mapped trace of the LVF (along the western margin of the Coast Range rather than occurring along the eastern margin of the Central Range). The apparent disparity between the source of the earthquake and initial reports

of surface rupture distribution along an adjacent but separate fault with an opposing dip direction raised questions about the role of coseismic triggered slip on creeping faults. As such the team focused much of their effort on evaluation the extent and magnitude of slip distribution associated with the LVF.

Three full days of field reconnaissance were dedicated to evaluating the distribution and effects surface fault rupture from October 18th to October 20th, 2022 (Figure 4.1). Reconnaissance day one was focused on documenting surface rupture along the Chihshang segment of the LVF in the vicinity of Fuli and the Bieh River. Day two included a morning of continued reconnaissance along the LVF north of Fuli, observations of displaced farm rows south of Yuli, and an afternoon reviewing surface ruptures in Yuli. The morning of day three was dedicated to making additional observations of surface rupture in Fuli and interviewing town residents regarding the effects of the September 2022 and historical surface-rupturing earthquakes. The afternoon of day three was spent looking for surface rupture near the northern end of the Yuli fault south of Wuhe. Additionally, the surface rupture team used a partial fourth day on October 21st to guide subsequent drone surveys, document additional fault complexity in and around the Dongli Middle school, and review surface rupture south of Chihshang near Luye (Figure 4.1).

4.1 Chihshang segment of the LVF near Fuli and the Bieh River (Day 1)

The Fault Rupture Team arrived at 8:30 am at an under-construction side-road bounded on the west by a concrete retaining wall and on the east by the Highway 9 embankment, as shown in Figure 4.2. The exact location of the Chihshang Fault at this location is not known precisely, but it is estimated to be parallel to Highway 9 within 60 meters to the west. The highway at this location exhibited seemingly new cracking and right-lateral offsets, as shown in Figure 4.2. The under-construction road shown in Figure 4.2 drops in elevation by approximately 3 meters. This location was part of a broad area of slope failure (Figures 4.2 to 4.7) that occurred coincident with the west-facing scarp of the LVF several km south of Fuli (Figure 4.1). The site was under construction as part of project to widen Highway 9 towards the west and closer to the existing rail line. The location of the new road construction was generally coincident with the west-facing LVF escarpment, with new construction possibly burying the scarp.

The team documented displacements of the large (≥ 7-m-high) retaining wall shown to the west in Figure 4.2. The retaining wall was composed of 20-m-long sections. Table 1 quantifies the relative vertical and horizontal displacements between the wall sections. Most joints connecting 20-m-long wall sections displayed evidence of primarily wall-normal-displacement. Wall-parallel extension was also observed but less-common (Figures 4.4 and X-5). Displacements between wall sections were mostly a few centimeters to up to 10 cm. The wall connections between each section were buffered by foam padding above the cold joints, as shown in Figure 4.5. The sections were also connected by a stiff plastic that local construction workers informed us were originally meant for seepage control. This plastic deformed significantly due to relative displacements of the wall sections, as shown in Figure 4.5. Coincidence with the primary fault trace complicated initial interpretations of whether displacements of the wall and adjacent ground cracking were related to slope failure/loss of shear strength, fault displacement, or a combination of both.

Table 1: Measurements of Displacements between Wall Sections adjacent to Highway 9

Location Index	Right-Lateral (RL) or Left-Lateral (LL) Offset	Gap Width	Vertical Displacement Relative to Previous Wall	Distance to Next Joint
A (Northernmost Location)	RL 10 cm	5 cm	3 cm	15.4 m
B	RL 5 cm	1 cm	-2 cm	20.4 m
C	RL 4 cm	8.5 cm	+11 cm	20.4 m
D	LL 3 cm	1 cm	-2 cm	20.2 m
E	LL 2 cm	9 cm	+1 cm	20.6 m
F	RL 2 cm	2 cm	+1 cm	22.1 m
G	LL 2 cm	0.5 cm	+4 cm	18.0 m
H	RL 2 cm	4 cm	+2 cm	19.2 m
I	LL 4 cm	0 cm	+1 cm	20.0 m
J	LL 1 cm	2 cm	0 cm	20.0 m
K	LL 3 cm	2 cm	-1 cm	20.0 m
L	0 cm	2 cm	-4 cm	20.1 m
M	LL 6 cm	2 cm	-2 cm	20.0 m
N	0 cm	0 cm	+2 cm	20.0 m
O	0 cm	0 cm	0 cm	20.0 m
P (southernmost section)				

It was ultimately hypothesized that ground cracking was primarily the result of slope failure/lateral spreading. One local resident informed us that cracks opened up on their property during the earthquake's mainshock. One of these cracks, shown in Figure 4.7, was located in the floor of a garage only a few meters from a river canal and appears to have been previously opened and repaired (Figure 4.7b). Ground cracks were nearly all consistent with subsidence and or lateral spreading to the west. Vertical deformation of horizontal planar surfaces such as the existing roadway and compacted embankment was almost always associated with the DTW extension/tension cracks rather than shortening or sinistral displacement, as might be anticipated if deformation were primarily related to surface fault rupture. However, surface fault deformation

could not be precluded here, but it does not appear to have been the primary cause. In general, areas of slope failure observed by the team were commonly coincident with the fault trace.

Several faults are mapped within the Coast Range east of and roughly parallel to the LVF. The surface trace of the west-dipping Yungfong fault (backthrust to the LVF) is located about 2.7 km east of the LVF and represents the contact between the Lichi Mélange to the west and Fanshuliao Fm. mudstone and sandstones to the east. If the fault dips west at ~45° (interpreted as 42° by Gray, 2007) then the postulated intersection of the Yungfong fault and the LVF occurs at depths no greater than a few kilometers. The east-dipping Tuluanshan fault is located about 3.7 km east of the LVF (~1 km east of the Yungfong fault at the surface) and juxtaposes Miocene Tuluanshan volcanics over the younger Fanshuliao Fm. in a reverse sense. To address the potential for triggered displacement, the reconnaissance team completed a cursory survey along Road 23 and in the Bieh River drainage southeast of Fuli, using the road as the primary strain gauge.

No evidence of cracking and/or displacement of the roadway was observed along the Yungfong fault, suggesting that little no displacement was triggered by slip on the adjacent LVF. Similarly, for the well-located Tuluanshan fault, no clear evidence of fault deformation crossing the roadway was observed. If slip on either Yungfong or Tuluanshan faults was triggered by strong ground shaking and/or LVF displacement, then it was likely distributed and/or below the threshold required to produce clear evidence of displacement across road. Likely owing to the steep nature of the road cut and adjacent antecedent ravine, evidence of minor rockfall was observed along Road 23 at several locations directly east of the Tuluanshan fault. At this location the road is cut into the deeply incised canyon walls within the resistant Tuluanshan volcanics, shown in Figure 4.8.

4.2 Fault Rupture in the town of Fuli (Days 1 and 3)

The small town of Fuli is located approximately 6 km north-northeast of Chihshang, along the primary strand of the LVF where the Bieh River crosses the fault. Surface rupture and it's effects were well expressed in the town (Figures 4.9 to 4-19). Here, vertical uplift along the LVF is expressed as a prominent west-facing scarp crossing the town in a north-south direction and in flights of fluvial and strath terraces along the Bieh River (east of the fault) that have been uplifted at a rate likely greater than 10 mm/yr (Gray, 2007). Where Road 23 crosses the modified scarp of the LVF we observed numerous fault rupture features including two distinct zones of deformation along the primary scarp (Figure 4.10).

The elderly owner of a home adjacent to the scarp indicated that the lower of the two zones (at the west edge of the Road 23 intersection) has repeatedly ruptured during notable earthquakes on the LVF (1951, 2003, March 2022) but that no new deformation was observed following the September 2022 earthquakes. The upper zone (~10 m east) was the locus of September 2022 deformation and caused significant damage to structures along strike, although it is not known if this strand was involved in the earlier historical events. The March 2022 deformation on the lower zone was expressed as ~5 cm of shortening (see photo of painted asphalt) that the county had not repaired. The upper zone near the Road 23 intersection displayed 18 cm of pure sinistral slip, as indicated by offsets of pavement markings. Deformation to the north was more complex and produced buckling of asphalt in the roadway together with damage to sewer lines, retaining walls, building foundations, and concrete walkways.

A discrete offset of a house foundation corner north of the intersection displayed about 14 cm of heave and 2 cm of vertical separation (Figure 4.12). The fault at this location continued north beneath the house which was yellow-tagged. The adjacent attached building was severely damaged and red tagged (Figure 4.13). The front steps and back half of the house both subsided, suggesting a pop up, perhaps related to a small right (restraining) bend/step beneath the house. The fault strand continued to N and passed through other concrete and brick structures resulting in significant damage (Figs. 14-15). The alleyway between structures shown in Fig. 15 shows that the fault trace passed along the edge of a storm grate (shown in Figure 16) before continuing through the adjacent property, causing compressional damage shown as upheaval of the concrete in Fig. 17 and buckling of steel braces in Fig. 17. Figure 18 shows additional damage on the property that the property-owners informed the team occurred during the mainshock. Some of the offsets between structure and foundation, particularly Figure 18a and Figure 18b, according to the property owner, were the result of creep over time but approximately 2/3 of the offset occurred on September 18 alone. Another resident of this property informed the team that the same fault ruptured through the property during the 1951 earthquake.

The team tracked a continuation of the strand as a series of mm-scale cracks uphill toward the Fuli high school. The orientation of the fault continuation was roughly 90 degrees to the scarp and extended for at least 200 m. The series of cracks followed by the team is documented in Figure 4.19 leading towards Fuli Junior High School. Some of the cracks and observed damage are not verified to be related to the September 18 earthquake or not. Figure 4.20 shows additional earthquake-related damage to Fuli Junior High School inside the classrooms, and Figure 4.21 shows damage to a stairway and bridge leading to the school's track and field. The damage shown in Figure 4.21 appears to have been produced by relative extensional displacement between the school building and the anchor point of the bridge and stairway on the track and field side of the campus. This is evidenced by the gap in the bridge in Figure 4.21a, and the offset of the rebar in Figure 4.21f suggests about 5 cm of relative vertical displacement.

South of Road 23, several streets cross the geomorphic escarpment perpendicular to the fault (Figures 4.22 through X-24). Together with retaining walls and adjacent sewer lines, these streets provided ideal lateral strain gauges to assess net lateral displacement across the fault. Estimates of net lateral displacement across the fault range from 18 cm of the discrete offset to ~ 60 cm of offset of a sewer line over a zone 6 to 8 m wide. Lateral offsets of rice rows south of town on a Bieh River terrace are estimated to be approximately 50 cm (using a "standard" rice row width of 25 cm) over a width of several meters. Larger offsets of retaining walls and street margins could be related to long-term lateral creep, although the contribution from the long-term creep signal is unknown (as of the time of reporting).

4.3 Yuli ruptures (south and across the town): Day 2

Surface rupture reconnaissance for day 2 was focused on: 1) understanding fault rupture in the area near the northern terminus of LVF rupture and the southern Yuli fault rupture together with reviewing areas in Yuli City with prior historical rupture from the 1951 Longitudinal Valley earthquake sequence. The surface rupture team was joined by Academia Sinica professor Kuo-Fong Ma and her students for the reconnaissance in Yuli City.

The surface rupture team documented a zone of surface rupture and structural damage along a section of the LVF located roughly equidistant between Fuli and Yuli where the fault produces a

localized zone of apparent uplift manifest as a fault parallel ridge bisected by an antecedent drainage with uplifted fluvial terraces along its margins. Near the northern end of the ridge, the team observed several failures of concrete roadways, patios, and retaining walls (Figures 4.25 through 4-27). The damage observed on the properties shown in Figures 4.25 through 4-27 is not certain to be directly a result of fault rupture and could potentially be a result of seismically-induced slope displacement given that the properties are located on a slope (Figure 4.25).

At this location, displacement in the soil was largely concealed by complex buckling of concrete structures and slope failure but locally expressed as east- to east-southeast-vergent shortening in fault-perpendicular retaining walls, as demonstrated in Figures 4.26 and 4-27. The continuation of the crack in the pavement through the brick wall in Figure 4.26a suggests possible surface fault rupture, but the buckling of the pavement in Figure 4.26f suggests larger-scale slope displacement. However, the shortening was direction opposite that of west- to northwest-vergent slip on the primary strand of the LVF (as observed several kilometers north) and indicative of deformation related to triggering of a backthrust on the LVF. Figure 4.27a shows compression of the pavement around the property foundation on the south side of and adjacent to Dongning Street. Figures 4.27b-e show damage along the outer concrete wall of the property, including uplift of about 10 cm and extension of about 3 cm on the east boundary of the property (Figure 4.27b) and a 2mm wide crack in the wall on the south side of the property (Figure 4.27e). Figures 4.27f-i shows relative displacement between the foundation of the house and the surrounding property pavement confirmed to have been a result of the September 18 earthquake by the property owner. Figures 4.27j-k show additional cracking and wall buckling consistent with slope movement at this site.

4.4 Dongli Middle School: Day 4

Surface ruptures at Dongli Middle School provided the most comprehensive view of distributed triggered surface deformation across the fault zone, likely due to large swaths of land with mostly roads, well-maintained planar grassy fields, and a sports track; all of which served as excellent strain gauges to identify and measure surface displacement (Figures 4.28 to 4-35). In contrast to surface faulting observed in the Fuli where deformation was concentrated along the geomorphic escarpment in a zone that was mostly 10-m wide for less, surface ruptures at Dongli Middle School were distributed over a zone that ranged from 225 to nearly 400 m wide. Although the area is heavily modified for the school and roadways, much of the faulting near Dongli Middle School occurred in areas tens to more than 100 m from the geomorphic escarpment. Associated faults are likely to have been challenging to identify prior to the earthquake.

From field observations and subsequent review of the drone survey, we identified 29 separate fault strands ranging in length from 6 m to at least 80 m. All but one of the strands produced a small scarp or structural deformation indicative nearly pure shortening (e.g., Figure 4.30), with fault strike ranging from 020° to 032°. Individual scarp heights ranged from several centimeters to approximately 20 cm. In the area of the sports track and intervening field, numerous small scarps (including east-vergent strands) were distributed over a zone up to 65 m wide. A single strand with sinistral slip displaced a 1-m-thick reinforced concrete retaining wall and adjacent asphalt roadway 25 to 29 cm along the bridge approach east of the highway. Notably, the strike of the fault across the roadway was approximately 355°; 25° to 37° counterclockwise of those associated with reverse fault ruptures. The transition to primarily sinistral displacement is

consistent with a counterclockwise change in strike based on the overall west-northwest motion of the hanging wall (Coast Range) of the LVF.

4.5 Multiple historic surface ruptures at Yuli

The town of Yuli represents one of a handful of places on earth with multiple historic surface ruptures documented with photographs. The surface rupture team visited Yuli to review ruptures (Figures 4.36 to 4.42) that occurred through the central and northern parts of the city, including the site of the former Yuli Elementary School and track documented in the Shyu et al. (2007) reevaluation of the 1951 Longitudinal Valley earthquake sequence. In general, the location, sense of slip, and displacements amounts from the 2022 earthquake appear to be very similar to the 1951 Yuli rupture. Offsets at the school and track area appeared to be aligned with the 1951 ruptures through the track, sense of slip was nearly pure strike slip (as in 1951), and displacements typically ranged from 5 to 20 cm, similar to displacements of 10 to 40 cm reported by Shyu et al., 2007. Observed surface rupture was manifest as throughgoing linear faulting and localized zones of Riedel shears producing en-echelon tension cracks. Figures 4.36 and 4.37 show cases of the surface fault rupture trace intersecting the edge of a storm grate, similar to the intersection with the storm grate shown in Figure 4.16 in Fuli. These similar cases suggest that fault rupture is emerging along the weakest locations of the ground surface, i.e., along the discontinuity in the ground surface represented by the perimeter of the storm grate, when such a location is available.

4.6 Takeaway points on surface rupture

1. Fault deformation was complex and rarely with oblique sinistral slip. In most instances, displacement along the LVF was expressed as either nearly pure sinistral strike slip (mostly in Fuli) or nearly pure shortening (Dongli), at least where offsets could be clearly defined. Where localized changes in fault strike were observed, sense of slip was strongly influenced by these geometry changes.
2. Although the M 6.9 earthquake is well documented to have occurred on the Central Range/Yuli fault, in the region between Chihshang and Dongli School the event resulted triggered slip along the LVF only.
3. As is commonly observed, surface ruptures for the M 6.9 September 2022 earthquake were strongly influenced by the built environment. Faults consistently followed structural weaknesses where they encountered manmade structures. This manifested as fault rupture intersecting the edges of building foundations or along the edges of storm grates.
4. Multiple locations with surface rupture documented during the 1951 earthquake and subsequent events re ruptured in September 2022. In Yuli, the position, sense, and magnitude of displacement were similar, whereas along the LVF, offsets were apparently much smaller than 1951. The latter observation is consistent with triggered rather than primary displacement during the 2022 earthquake.
5. Existing morphology proved to be an inconsistent predictor of fault rupture position. In Fuli, rupture locations are likely to have been predicted within a few meters to a few tens of meters. In contrast, ruptures at Dongli school would have been very difficult to predict and design for without prior subsurface fault investigation and exposure.

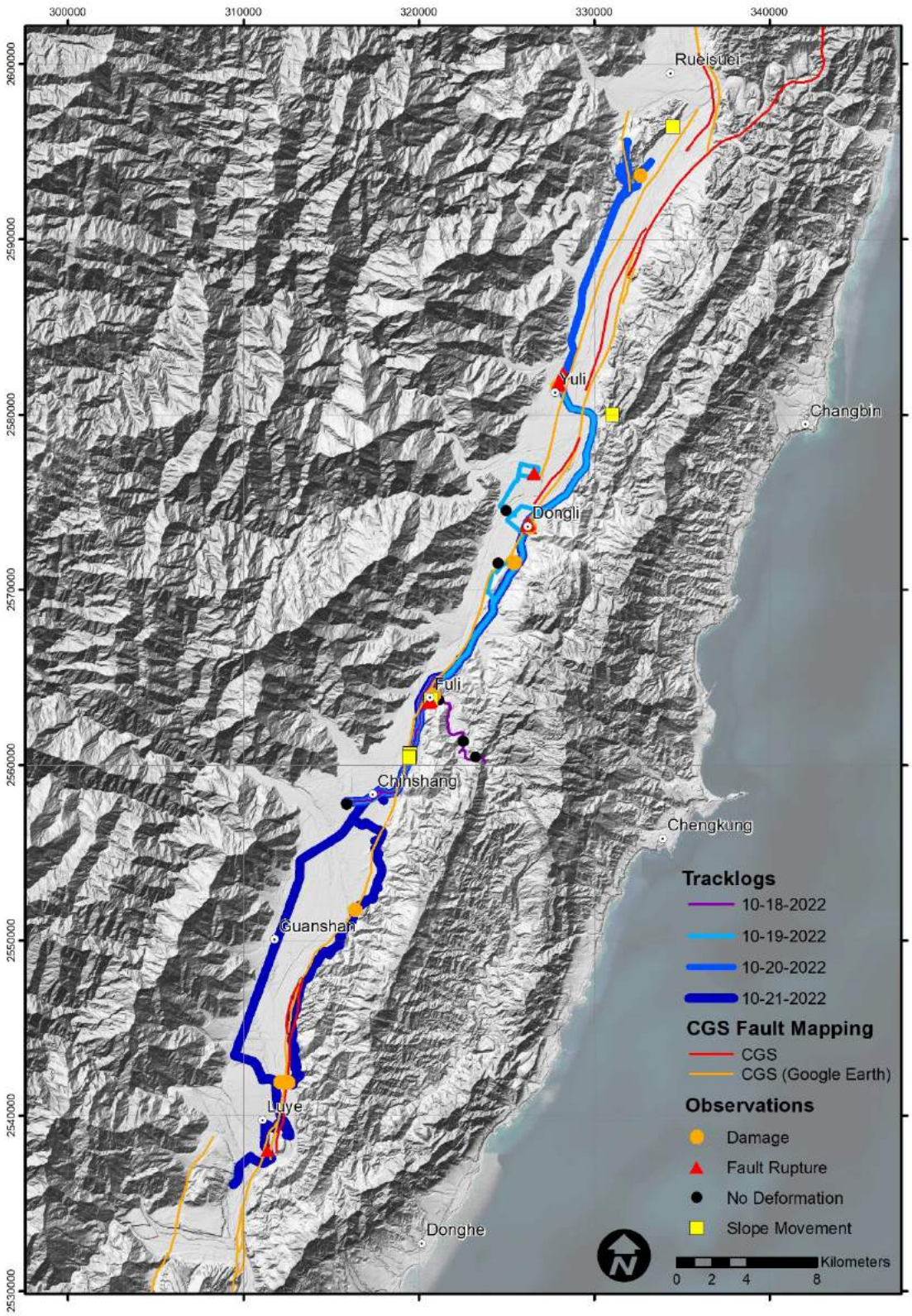

Figure 4.1: Tracklog and observation map from the surface fault rupture team.

(a) (b)

Figure 4.2: (a) Extension and subsidence of highway related to failure of adjacent retaining wall under construction in upper right corner. View looking north. (b) Extension and subsidence of highway related to failure of adjacent retaining wall under construction. View looking south with retaining wall right (west) of image. Lat: 23° 8’ 36.82248”, Lon: 121° 14’ 12.564599”.

Figure 4.3: View looking south along retaining wall showing displacement of joint between 20-m wall sections. Backfill composed of river gravel, locally emplaced in lifts between geotextile. Lat: 23° 8’ 43.47456”, Lon: 121° 14’ 13.727399”.

Figure 4.4: View looking west showing separation of joint between 20-m wall sections. Lat: 23° 8’ 44.762279”, Lon: 121° 14’ 14.010719”.

(a) (b)

Figure 4.5: Views looking (a) south and (b) west along retaining wall showing displacement of joints between 20-m wall sections. Lat: 23° 8’ 43.357199”, Lon: 121° 14’ 13.556040”.

Figure 4.6: View looking north and ground cracking areas “repaired” with concrete. Failed retaining wall in upper left. Lat: 23° 8’ 39.00048”, Lon: 121° 14’ 12.52428”.

(a) (b)

(c)

Figure 4.7: (a,b) Crack in garage floor adjacent to highway 9. This garage is located within only a few meters of a river canal shown in (c). Lat: 23° 8’ 35.48292”, Lon: 121° 14’ 12.83136”.

Figure 4.8: Roadside showing Tuluanshan volcanics.

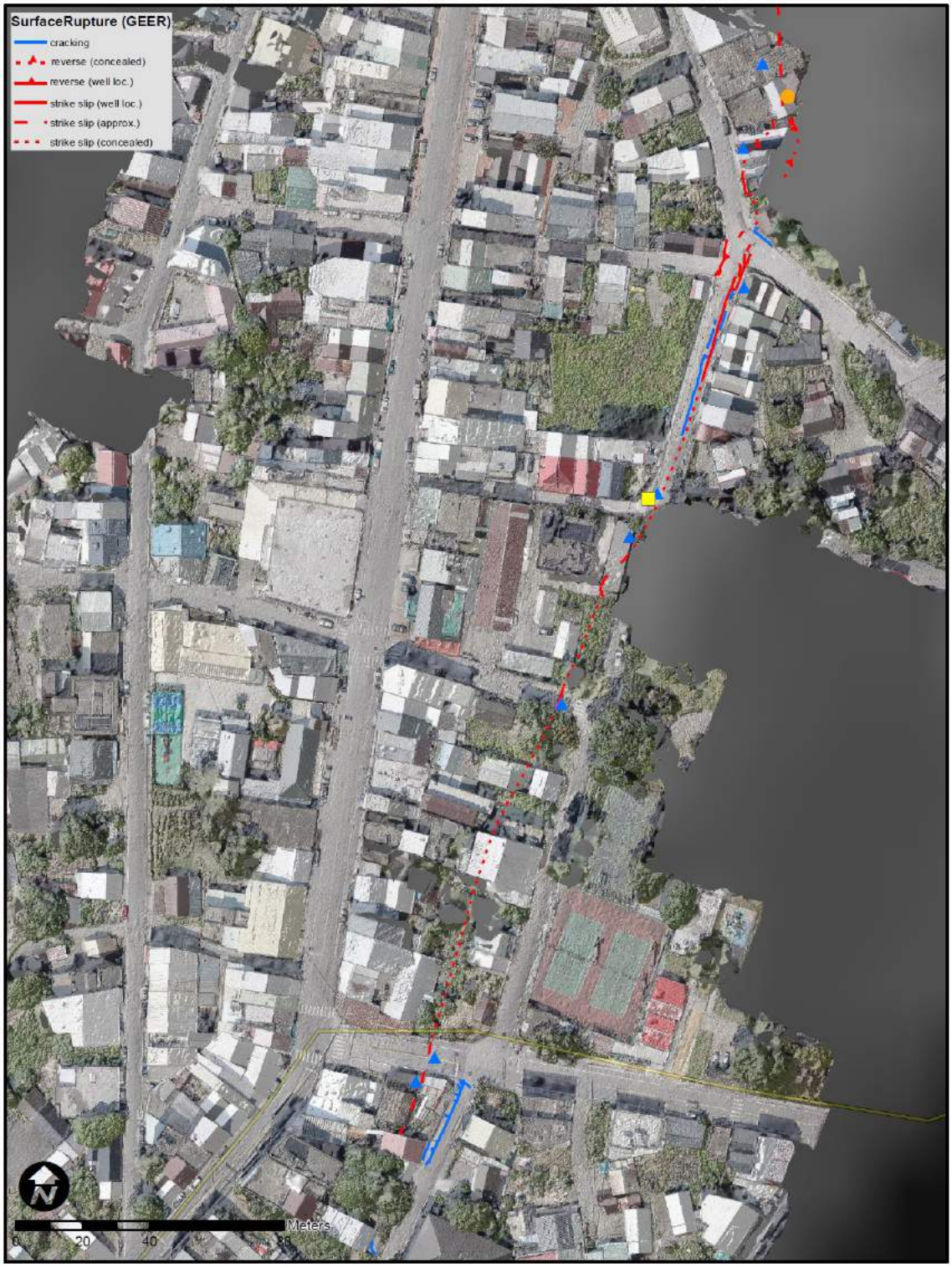

Figure 4.9: Rupture map in the town of Fuli.

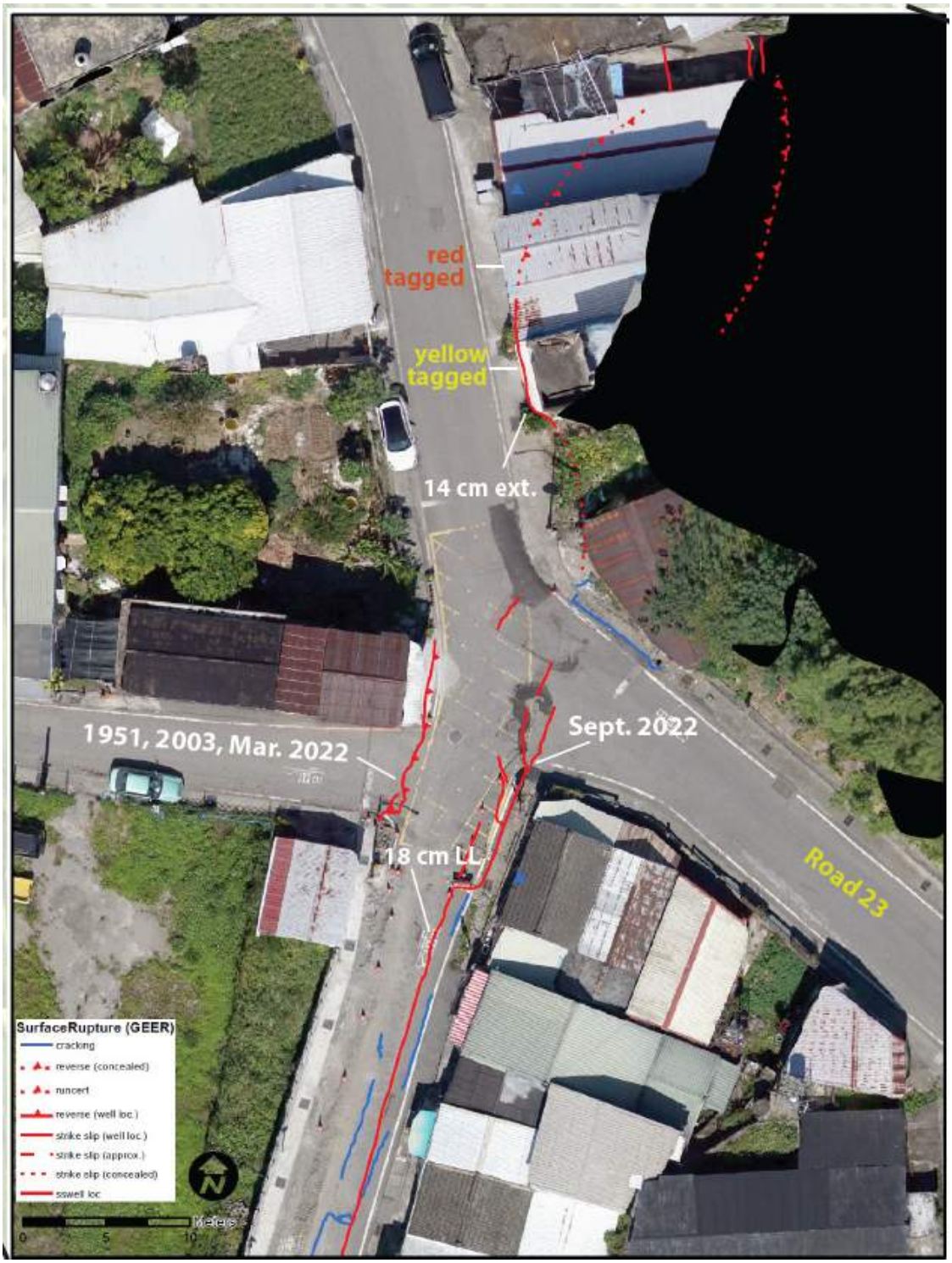

Figure 4.10: Detailed map of surface rupture at the Road 23 intersection in Fuli. Photos of structures north of the intersection are shown in figures below. Note position of September 2022 and prior surface ruptures at this location.

Figure 4.11: Surface rupture coincident with fault-parallel sewer line. Discrete LL offset is 18 cm. Lat: 23° 10’ 24.693599”, Lon: 121° 14’ 54.185999”

(a)

(b)

Figure 4.12: Fault rupture along a localized left (releasing) bend in the LVF. Rupture propagated around the foundation here but resulted in 14 cm of extension at the foundation corner. Lat: 23° 10’ 25.973039”, Lon: 121° 14’ 54.221279”

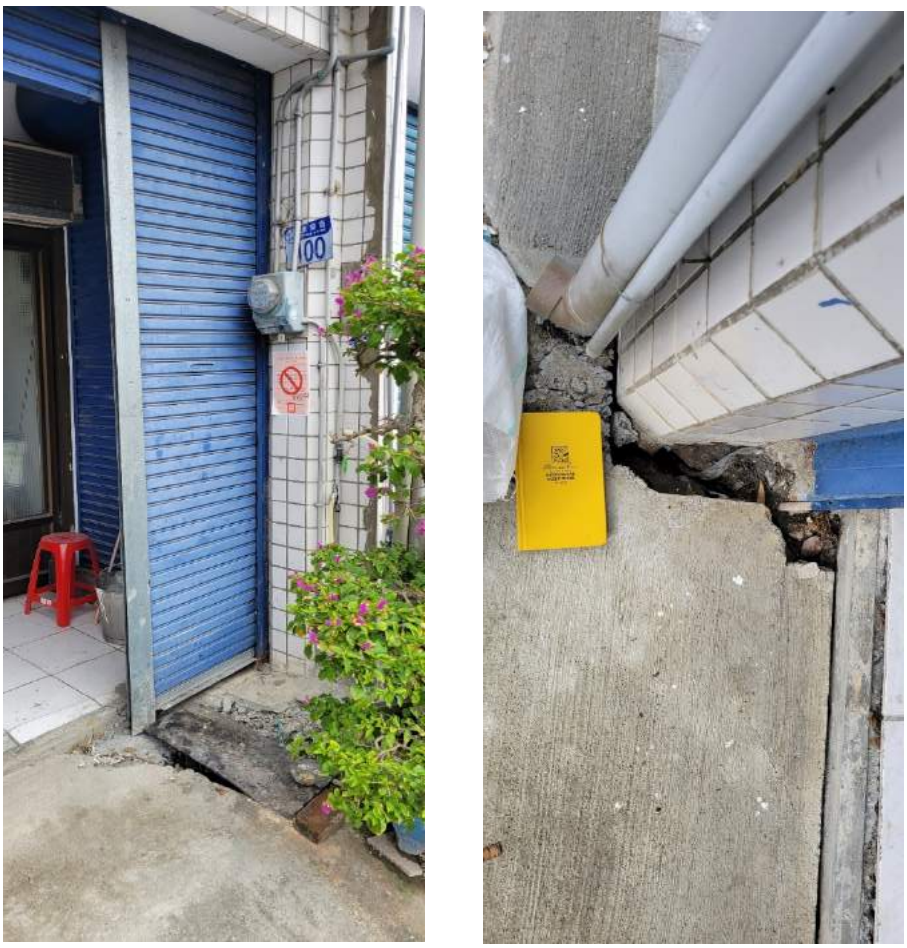

(a) (b)

(c)

Figure 4.13: Fault rupture along a localized left (releasing) bend in the LVF. Fault rupture propagated along the edge of this foundation here, adjacent to the structure shown in Figure 4.12. Lat: 23° 10’ 26.174639”, Lon: 121° 14’ 54.370679”

(a) (b)

Figure 4.14: Partial collapse of URM structure along the LVF. Rupture propagated beneath the house. Lat: 23° 10’ 26.201999”, Lon: 121° 14’ 54.605400”

(a)

(b)

Figure 4.15: Buckled concrete slab and brick building walls along the LVF scarp north of the Road 23 intersection. Lat: 23° 10’ 26.527440”, Lon: 121° 14’ 54.743639”

(a)

(a)

(b)

Figure 4.16: Surface rupture localized along weakness in concrete slab coincident with drain cover. Lat: 23° 10’ 26.527440”, Lon: 121° 14’ 54.743639”

Figure 4.17: Deformation of braced concrete structure built into the LVF scarp. Deformation was largely coseismic based on owner's account. Lat: 23° 10' 27.884280", Lon: 121° 14' 54.895199"

Figure 4.18 (a) Concrete damage due to relative foundation movement around water pipeline. Lat: 23° 10' 28.720199", Lon: 121° 14' 55.052159"

Figure 4.18 (b) Separation of concrete walls from foundation. Lat: 23° 10’ 28.626959”, Lon: 121° 14’ 54.975479”

Figure 4.18 (c) Cracking in concrete stairs resulting from relative foundation displacement. Lat: 23° 10’ 28.512480”, Lon: 121° 14’ 54.98628”

Figure 4.18 (d) Pavement buckling. Lat: 23° 10’ 28.520039”, Lon: 121° 14’ 55.023719”

(e) Relative movement of foundation. Lat: 23° 10’ 28.924320”, Lon: 121° 14’ 54.961080”

Figure 4.18 Additional damage due to relative foundation movement on a private property.

(a) Crack in pavement produced during mainshock. Lat: 23° 10’ 28.945920”, Lon: 121° 14’ 54.936599”

(b) View uphill following presumed trace of fault seen via cracks in pavement. Lat: 23° 10’ 28.918199”, Lon: 121° 14’ 54.926159”

(c) Hairline fracture in concrete wall uphill from (b). Lat: 23° 10’ 28.858440”, Lon: 121° 14’ 56.000759”

(d) Cracks in walkway between private property and Fuli Junior High School. Whether this crack was directly caused by the September 18 earthquake is uncertain. Lat: 23° 10’ 28.848720”, Lon: 121° 14’ 56.038199”

(e) View looking uphill from (d).

(f) Foundation offset with uncertain cause. Lat: 23° 10’ 28.041599”, Lon: 121° 14’ 56.212440”

(g) Inward buckling of concrete wall. Uncertain as to whether this was a direct result of the September 18 earthquake. Lat: 23° 10’ 28.223039”, Lon: 121° 14’ 56.014799”

Figure 4.19 Possible continuation of fault rupture uphill from Figure 4.17 towards Fuli Junior High School.

(a)

(b)

Figure 4.20: Diagonal cracks in walls of Fuli Junior High School classrooms presumed to have been caused by September 18 earthquake. Lat: 23° 10’ 30.607680”, Lon: 121° 14’ 56.832000”

(a)

(b)

(c)

(d)

(e)

(f)

Figure 4.21: Damage to bridge and stairway connecting main Fuli Junior High School building to the campus track and field. Lat: 23° 10’ 31.246680”, Lon: 121° 14’ 58.095959”

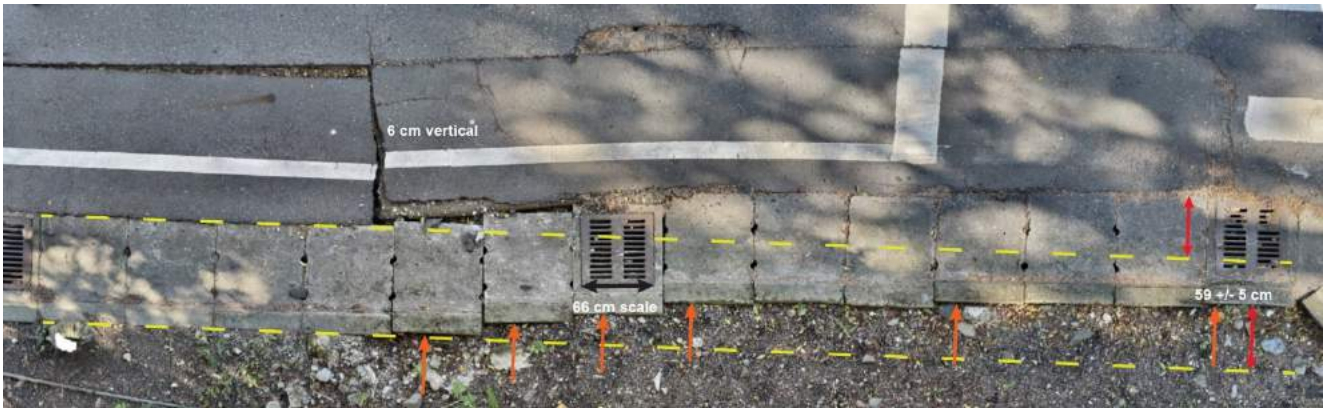

Figure 4.22: offset of sewer lateral in Fuli. The best estimate of total LL displacement is 59 cm, include possible pre-event creep and/or prior surface rupture on the LVF.

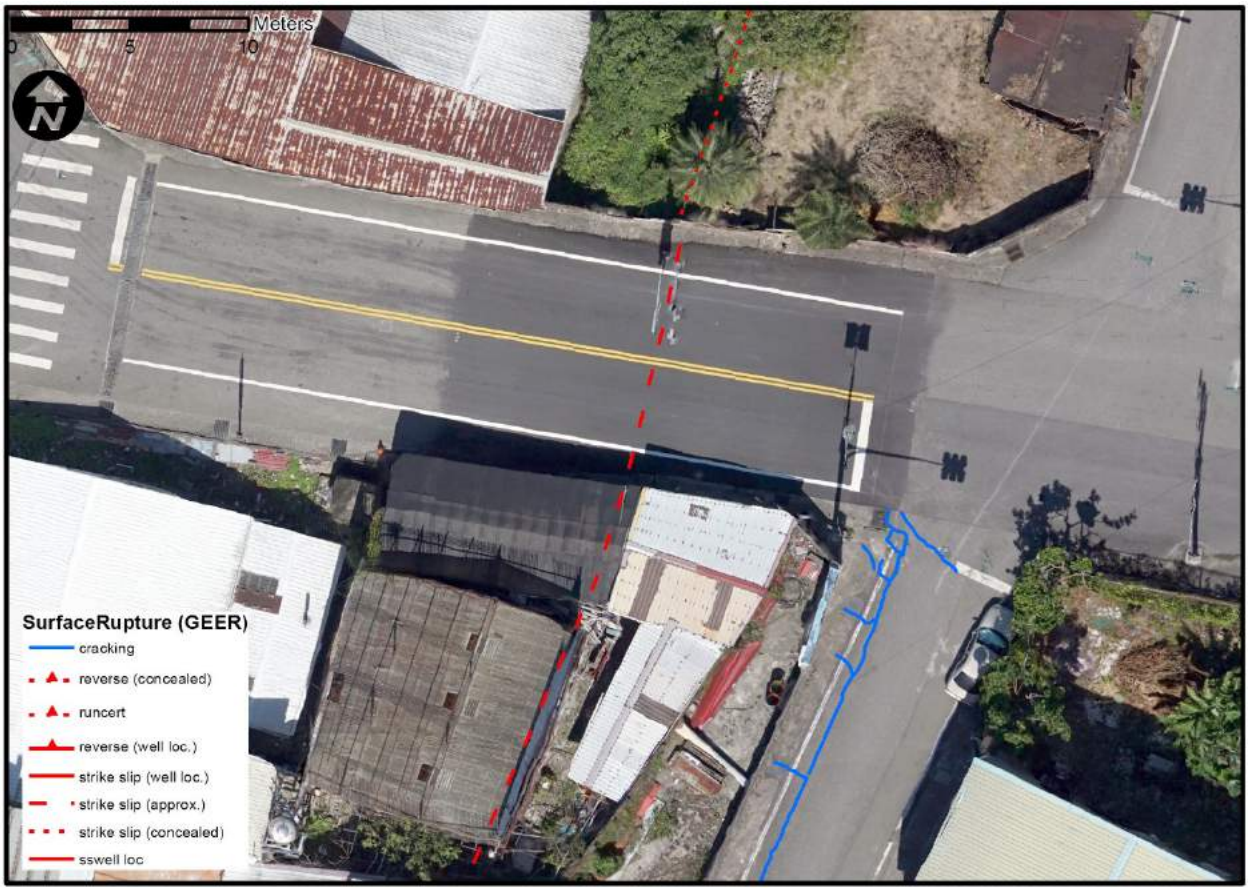

Figure 4.23: Map view of repaired intersection in Fuli. Sewer lateral and adjacent wall are sinistrally offset ~90 cm. Displacement may include pre-event creep and/or prior surface rupture on the LVF.

Figure 4.24: West-looking view of offset sewer lateral and brick wall. Total LL offset is ~90 cm, which may include creep and/or surface rupture on the LVF that occurred prior to the September earthquake.

(a)

(b)

Figure 4.25: Views looking (a) uphill and (b) downhill along Dongning Street adjacent to properties exhibiting recent damage. Lat: 23° 14’ 39.447239”, Lon: 121° 17’ 37.383720”

(a)

(b)

(c)

(d)

(e)

(f)

(g)

Figure 4.26: Damage associated with property on north side of Dongning Street. Lat: 23° 14’ 39.136920”, Lon: 121° 17’ 38.056919”

(a)

(b) (c) (d) (e)

(f)

(g) (h) (i) (j)

(k)

(l)

Figure 4.27: Damage associated with property on south side of Dongning Street. Lat: 23° 14’ 38.140800”, Lon: 121° 17’ 37.683600”

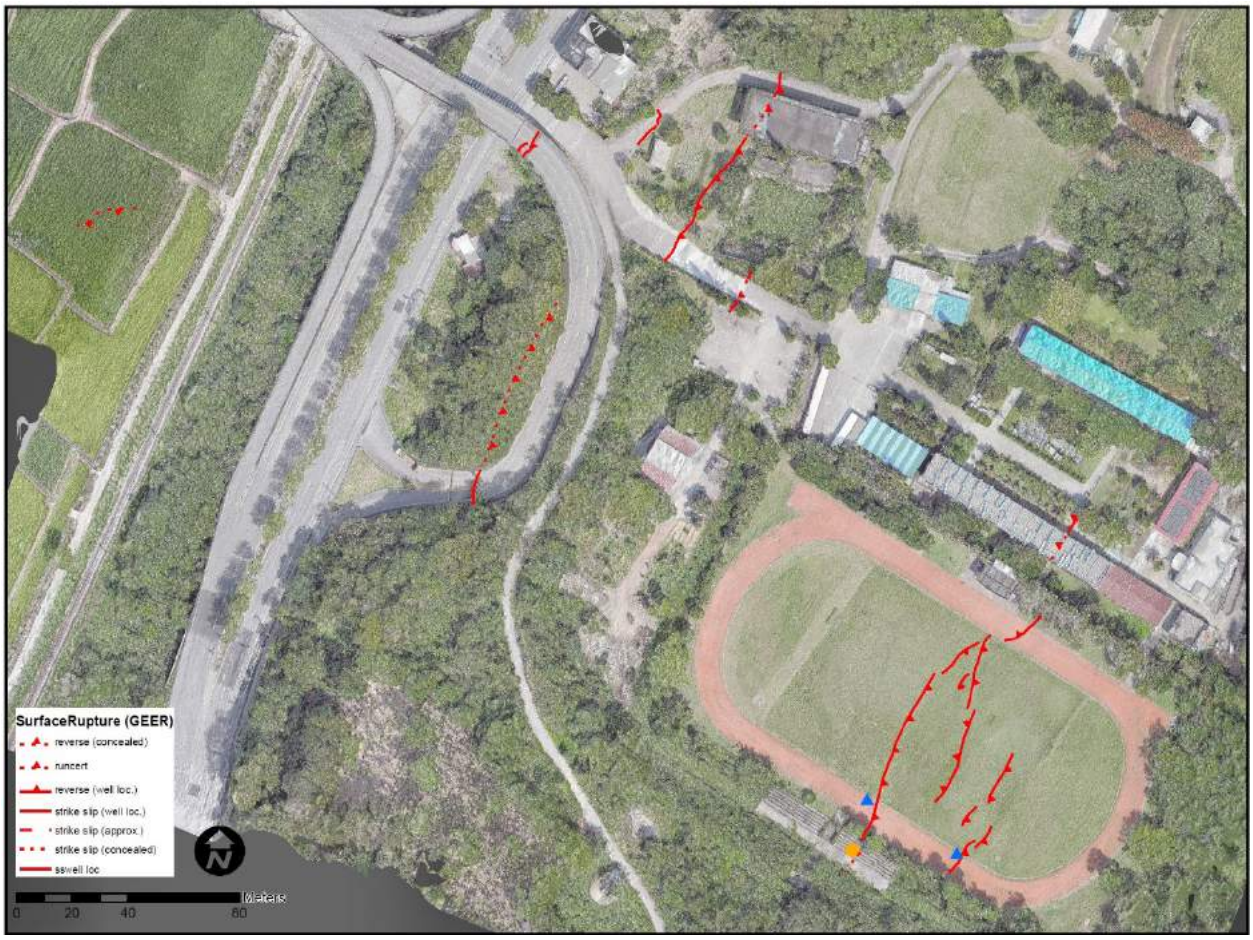

Figure 4.28: Surface Rupture Map at Dongli School

Figure 4.29: Reverse faults in the school athletic fault. Scarp height reaches a maximum of 13 across this strand, similar to others shown on the map above. Lat: 23° 15’ 44.124479”, Lon: 121° 18’ 7.791120”.

(a) Lat: 23° 15’ 43.836479”, Lon: 121° 18’ 8.961839”

(b) Lat: 23° 15’ 44.803440”, Lon: 121° 18’ 7.317719”

(c) Lat: 23° 15’ 46.403640”, Lon: 121° 18’ 9.362160”

Figure 4.30: Buckled concrete linings around inside perimeter of track at Dongli Middle School.

Figure 4.31: 14-cm reverse fault scarp located near the projection of the LVF, west of the school, Lat: 23° 15’ 46.403640”, Lon: 121° 18’ 9.362160”

Figure 4.32: Reverse faulting through unreinforced cobble and concrete retaining wall, Lat: 23° 15’ 46.403640”, Lon: 121° 18’ 9.362160”

Figure 4.33: Damage to structure on the opposite side of the street from the retaining wall in the figure above. Cracking extends from the foundation to the roof, Lat: 23° 15’ 46.403640”, Lon: 121° 18’ 9.362160”

Figure 4.34: Surface rupture through the bridge approach near projected location of the LVF. Asphalt pavement buckled and locally detached. View looking southwest, Lat: 23° 15’ 46.403640”, Lon: 121° 18’ 9.362160”

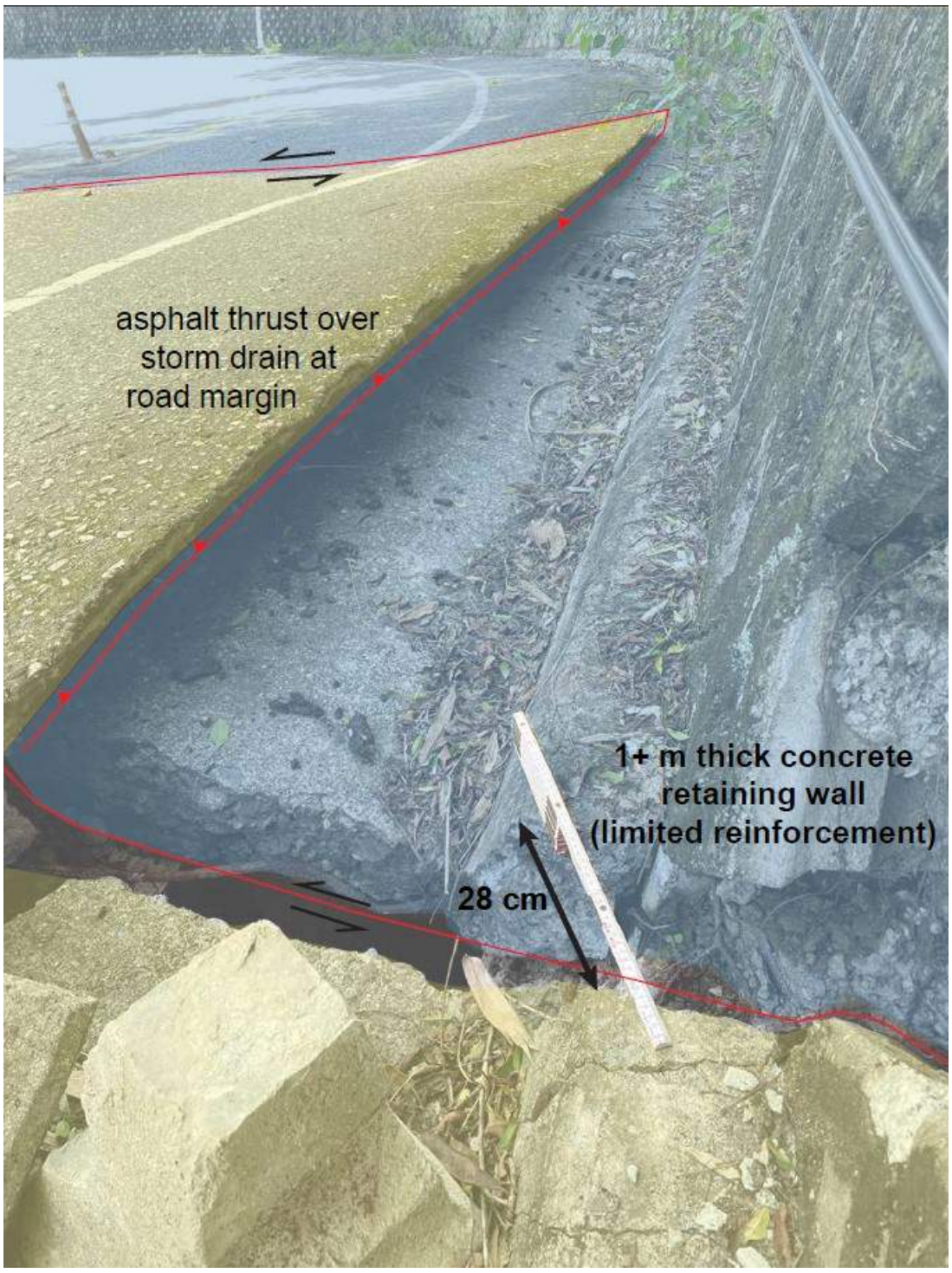

Figure 4.35: Annotated photo showing view of buckled pavement on bridge approach. Net horizontal displacement of the 1-m-thick concrete retaining wall (sparse reinforcement) was ~28 cm, Lat: 23° 15’ 46.403640”, Lon: 121° 18’ 9.362160”

(a)

(b)

(c)

Figure 4.36: Minor (<10 cm) offset of storm drain across the Yuli fault. Location Roughly coincident with 1951 Rupture (Shyu et al., 2007). Lat: 23° 20’ 10.720679”, Lon: 121° 19’ 1.702919”

(a) (b)

Figure 4.37: Displacement of sidewalk pavers on the north side of the former Yuli Elementary athletic field. Left lateral displacement is ~11 cm. (a) View looking west. (b) View looking north. Lat: 23° 20’ 12.623999”, Lon: 121° 19’ 2.764200”

Figure 4.38: Left lateral offset across the Yuli fault north of the town center.

Figure 4.39: Red-tagged structure along path of fault trace. Lat: 23° 20’ 20.139000”, Lon: 121° 19’ 2.544479”

Figure 4.40: En-echelon tension cracks with apparent ejected sands at the Yuli High School athletic field. Lat: 23° 20’ 31.165800”, Lon: 121° 19’ 11.031959”

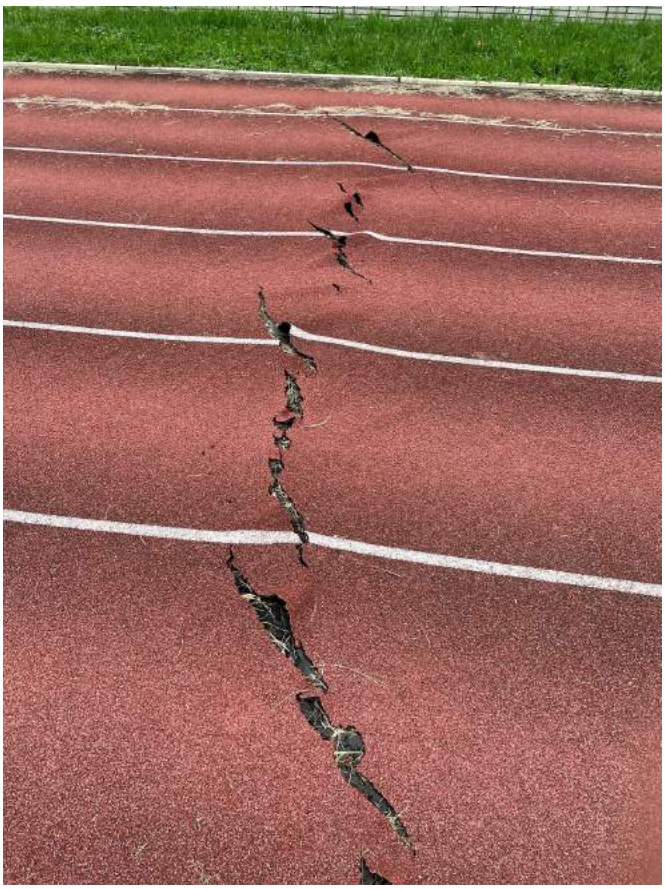

Figure 4.41: En-echelon tension cracks rupturing the track at the Yuli High School athletic field. Lat: 23° 20’ 31.715519”, Lon: 121° 19’ 11.219520”

5. OBSERVATIONS OF BRIDGE DAMAGE

This section documents the GEER/NCREE team's observations of bridge damage in the Longitudinal Valley following the M6.5 and M6.9 earthquakes. It was not possible to do a completed assessment of bridge states and/or damage in the 16 hours between earthquakes. However, any significant damage from the M6.5 earthquake that would have impacted the use of the bridges would have been noted before the M6.9 event. The only damage attributed to the M6.5 earthquake was to the Baohua bridge, and all other damage is assumed from the M6.9 event. The bridge damage team was led by Trevor Carey.

5.1 Longitudinal valley bridges

Light to heavy damage was surveyed in eight bridges as part of the reconnaissance mission. The locations of the five most heavily damaged bridges along the trace of the Longitudinal Valley fault (LVF) and M6.9 epicenter are given in Figure 5.1. Ground motion recordings near the bridges are also provided. All the bridges were located within 2 km of the fault due to the narrowness of the valley, but none of the bridges were identified as crossing the LVF, which would have made them susceptible to damage from fault offset. Overall, two bridges had multi-span, and foundation pier collapses, three were closed for repair, and the remaining bridges were operational but with reductions in service.

The ground motion recordings in Figure 5.1 show a velocity pulse intensified northerly along the fault and in the direction of rupture. These directivity effects placed greater seismic demands on the bridges at the northern end of the valley than the undamaged bridges south epicenter. The displacement time histories include permanent displacements caused by fault offset using the procedure described in the ground motion section of this report.

The GEER team did not observe indicators of ground failure at any of the bridges surveyed that would suggest liquefaction was triggered, and damage to the bridge foundations and superstructure elements is not assumed to be from ground failure. The lack of ground failure was consistent with observations of limited ground failure throughout the valley. The initial NCREE reconnaissance teams surveying damage shortly after the M6.9 event also did not find any evidence of ground failure.

5.1.1 *Baohua Bridge (Built in April 1984)*

The Baohua Bridge (22.97500°, 121.16860°) is a 680 m long reinforced concrete deck girder bridge with 18 spans supported by pier foundations, oriented in the east-west direction over the Beinan River. Damage to the bridge occurred during the M6.5 earthquake, confirmed by a United Daily News report of the damage (https://udn.com/news/story/123028/6620894?from=udn-relatednews_ch2), and published before the M6.9 event. The bridge was operational but had reductions in service due to ongoing repairs during the GEER visit. Damage was primarily a transverse offset of two spans near the east abutment, causing buckling (Figure 5.2) of the road asphalt surface and failure of the metal guard rail at the adjoining spans. The approximate transverse offset gap between the concrete barriers shown on the left side of Figure 5.2b is 51 cm. Figure 5.3 is an additional view of the offset but looking back towards the east abutment. Figure 5.4 is a photo of the expansion joint damage. There was no offset in Figure 5.4 due to the larger pier caps to support the wider road deck for a traffic pull-off. The bridge did have a seismic

retrofit at each of the piers to provide additional longitudinal bearing length to prevent longitudinal unseating (Figure 5.5), but no transverse shear keys or retainers were identified.

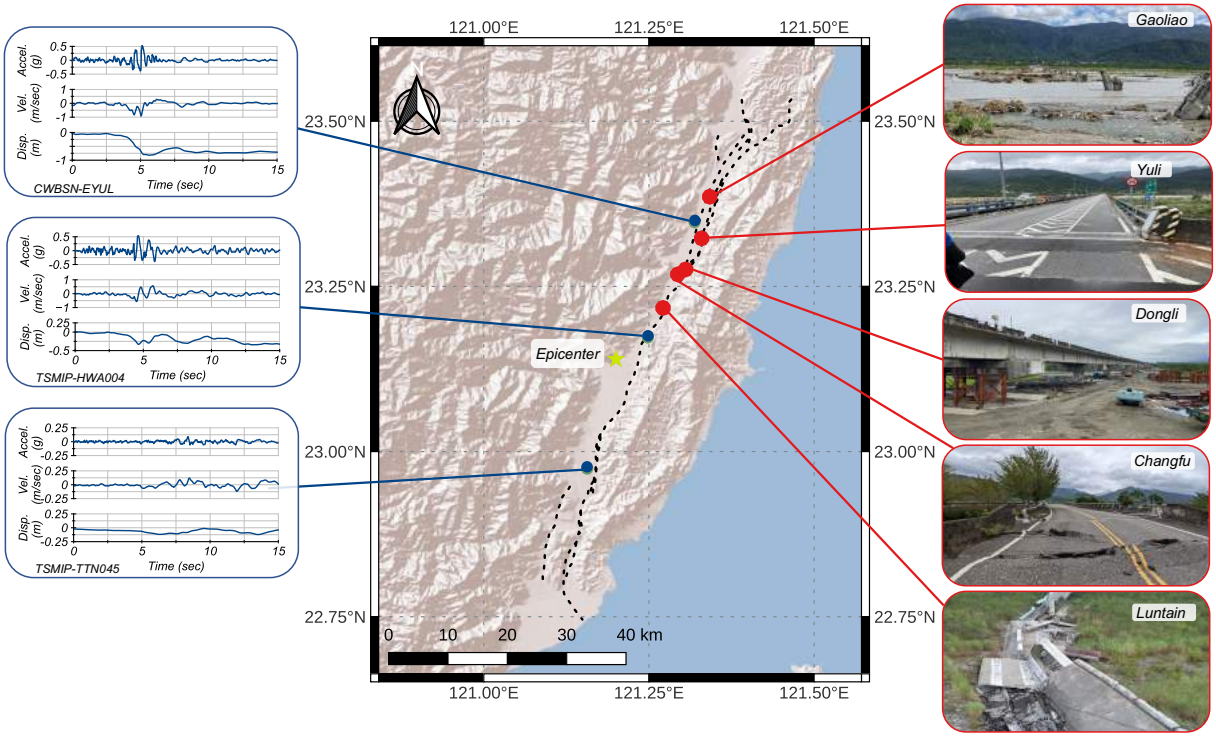

Figure 5.1. Locations of the five most heavily damaged bridges, the traces of the Longitudinal Valley Fault, the epicenter of the M6.9 earthquake, and select acceleration, velocity, and displacement time series from that event.

(a) (b)

Figure 5.2. a) Damage between adjacent bridge spans buckling roadway, concrete barrier, and metal guardrail (United Daily News), looking south; b) repaired roading and metal guardrail damage during GEER/NCREE visit looking northwest. (22.97480° 121.17020°)

Figure 5.3. Lateral offset, looking towards the east abutment. (22.97484° 121.17017°)

(a) (b)

Figure 5.4. a) View of bridge deck crack looking south; b) view of deck crack looking north (22.97485° 121.16941°)

Figure 5.5. View of typical retrofit by adding additional bearing area to prevent longitudinal unseating (22.97479° 121.17059°)

5.1.2 *Luntian Bridge (Built in June 1982)*

The Luntian Bridge (23.21790°, 121.27050°) is a 420 m long reinforced concrete deck girder bridge with 14 spans (@ 30 m length) supported by pier foundations. The bridge orientation was east to west and perpendicular to the LVF and the direction of rupture. The bridge width was 4.55 m wide, with one wider span for a traffic pullout. The seven continuous spans and supporting pier foundations closest to the west abutment failed during the earthquake (See Figure 5.6a). When the GEER team arrived in October, the concrete decks had already been removed, and only the failed piers remained (Figure 5.6b). The remaining seven spans did not fail but experienced yaw rotation and compression causing buckling of asphalt and/or abrupt offsets at the span joints at each pier cap. (Figure 5.7).

In each of the remaining seven spans, the deck girders laterally translated north, following the direction of the fault rupture. Figure 5.8 is a view from Google Street view looking at the 2nd pier from the east abutment, and Figure 5.9 is a photo from the same location taken by the GEER team. The concrete girder in Figure 5.9 was transversely shifted to the north by 60 cm, and unseating the girder from the elastomeric bearing pad (Figure 5.10). A 60 cm magnitude of offset was visually consistent with other remaining spans. Pier 2 in Figure 5.10 and the other spans near the east abutment had an additional longitudinal translation of the girders almost resulting in longitudinal unseating. The longitudinal translation of the girders was not uniform pier to pier, causing the bridge spans to rotate and buckle at the bridge deck. At pier 2 in Figures 8-10, no

transverse or longitudinal restraints were identified that would have prevented girder translation. At the other pier caps there appeared to be no restraints that restricted movement.

The failure of the seven west spans is assumed to be partly for the transverse unseating of the bridge girders from the top of the pier cap. Figure 5.11 is the last remaining span and pier foundation, with the north girder translated to the edge of the pier cap. The bridge deck and concrete girders were integrated, which produced an overturning moment at the base of the concrete pier and lateral sliding forcing on the remaining two girders that had not slid off the pier cap.

The pier foundations were roughly 4.42 cm from the base of the foundation to the bottom of the pier cap. None of the failed piers were deeply embedded beneath the ground surface, with average embedment depths varying from 0.5 to 1 m. The bearing soil varied from fined-grained to rounded large cobbles and boulders. While this soil may have been adequate for bearing capacity bridge loads, it may have also limited the embedment depth of the piers due to limitations of drilling or driving pile due to the larger particle sizes. A typical view of the rebar at the base of the pile is provided in Figures 11-13. The spacing between longitudinal rebar varied from pier to pier. The rebar was embedded into the ground surface at an unknown depth. The vertical spacing between shear reinforcing hopes was roughly 45 cm but could only be confirmed at one pier.

At least one of the pier foundations was bearing on a larger concrete bearing pad. One of the NCREE team members mentioned this construction practice is typical because scour at the foundation supports is a common type of bridge damage in the region. It is speculated the pier foundation and cap were cast at different times due to the smooth failure surface suggesting there was a concrete cold joint between the bottom of the pier and the top of the bearing pad (see Figures 13 and 14). The longitudinal rebar of the pier was socketed into the concrete bearing pad but was not sufficient to prevent failure.

(a) (b)

Figure 5.6. a) Failed spans and pier foundation supports at the Luntian Bridge (image curious of NCREE); b) view for concrete bridge piers after deck removal during GEER team visit in October 2022 (23.21726° 121.27172°)

(a) (b)

Figure 5.7. a) Looing from the east abutment west at asphalt buckling and offset of the bridge spans that did not fail. (23.21636°, 121.27356°); b) typical view of the span offset at one of the pier caps (23.21665° 121.27302°).

Figure 5.8. Looking west at the 2nd pier from the east abutment prior to the earthquake. Note the location of the utility pipes on the pier cap. Photo from Google Street View from 2012 (near 23.21457° 121.27268°)

Figure 5.9. Looking west at the 2nd pier from the east abutment following the earthquake. Note the north translation of the utility pipes from Figure 5.8. (23.21457° 121.27268°)

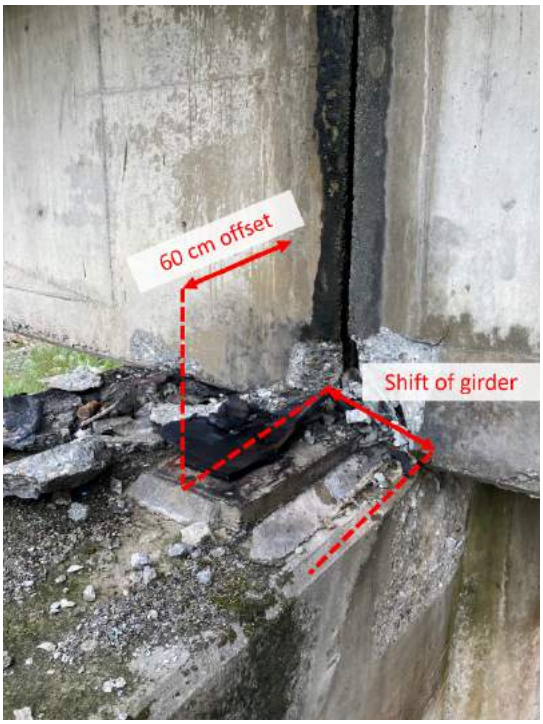

Figure 5.10. 60 cm transverse translation of the bridge girder north, and longitudal shift of the girder towards the east abutment. (23.21459° 121.27268°)

Figure 5.11. View from the bottom of one of the failed pier foundations. The longitudal rebar yeilded and reatlivilty smooth base suggesting a cold joint (23.21753° 121.27116°)

Figure 5.12. Typical view of one of the failed piers with irregular longitudinal rebar spacing. (23.21775° 121.27062°)

Figure 5.13. View of a failed pier with irregular longitudinal rebar spacing. Same pier as and concrete pad as Figure 5.14. (23.217653° 21.270928°)

Figure 5.14. View of failed bridge pier and concrete pad. Note the yield longitudinal rebar connecting the pier to the concrete pad. (23.21771° 121.25425°)

5.1.3 *Changfu Bridge (Built in November 1997)*

The Changfu Bridge (23.26872°, 121.29297°) is 1850 m in length, consisting of a series of main-span bridges, elevated approaches, and non-elevated sections. The main spans and elevated approaches were pre-stressed concrete girders supported by pier foundations. The abutments for the main spans and approaches were built-up earthen berms, retained by back-to-back cast-in-place concrete sections. Figure 5.15 is a Google satellite view of the east side of the bridge. The shaded regions delineate the elevated sections and built-up earthen berms. Figure 5.16 is a view looking west from the abutment, showing the prestressed deck girder, supporting piers, and built-up abutments. The longitudinal axis of the bridge is east to west, also making it perpendicular to the LVF and the direction of rupture. Concrete shear keys at the ends of pier caps (Figure 5.16), and the use of diagrams between girders prevented the bridge girders from transversely unseating. At the east abutment, there was a surface fault rupture that crossed the built-up earthen berm, which is described in the surface fault rupture portion of this report.

Damage to the main-span bridges and approaches was confined mainly to the expansion joints at the pier caps between adjacent spans. Resulting in offset of adjacent spans (e.g., 41 cm lateral offset between the double yellow lines in Figure 5.17 at the east abutment) gaps or pounding/compressional damage at the concrete and metal barriers (Figures 18-20). At the west abutment in Figure 5.21, the gap between the bridge elements and built-up berm was 25 cm, with the depth of the opening being the height of the bridge girders and integrated deck.

A common source of damage in the back-to-back concrete cast-in-place sections retaining the earthen berm was cracks or separation at almost every concrete cold joint (example shown in Figure 5.22). It's unknown if the joints were open or visible prior to the earthquake, but the gaps appear to have widened, evidenced by damage to the concrete and soil that spilled from the joints. The opening and closing of cold joints allowed the berms to deform at locations and perhaps prevented damage at other locations if the concrete walls were continuous without any defects.

Figure 5.15. Google satellite view of the Changfu Bridge with the built-up earthen berms (red) and main-spans and approaches (yellow).

Figure 5.16. Looking west at a bridge main span with a built-up earthen berm in the background. Note the concrete shear keys at the ends of be pier caps retaining the prestressed girders. (23.26477° 121.30019°)

Figure 5.17. 41 cm lateral offset between bridge span and abutment. (Asphalt buckling due to surface fault rupture) (23.26452° 121.30089°)

Figure 5.18. Damage to expansion joint, concrete and metal barriers (23.26557° 121.29901°)

Figure 5.19. Compression buckling of concrete barrier steel reinforcement (23.26584° 121.29836°)

Figure 5.20. Shear failure in metal guardrail bracket caused by compressional loads. (The expansion joint preventing tensile loading) (23.26568° 121.29870°)

Figure 5.21. Extension of bridge joint at the west abutment. Gap approximately 25 cm. (23.26574° 121.29864°)

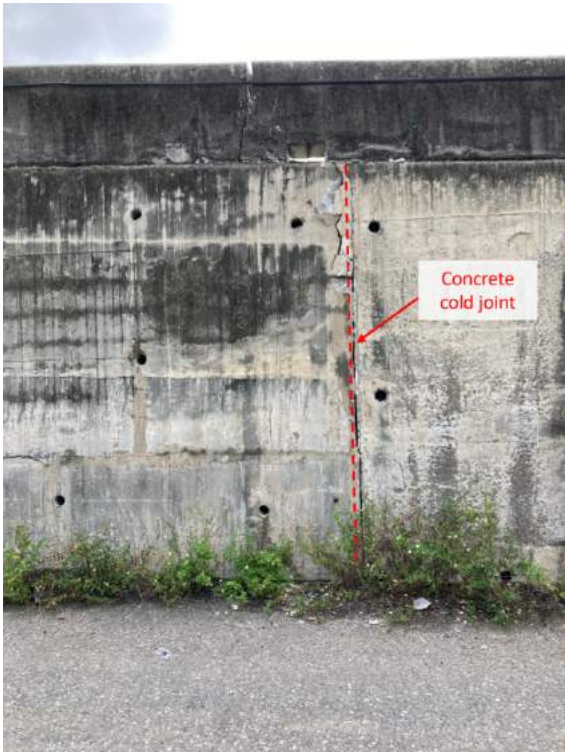

Figure 5.22. Typical cold joint in the cast-in-place concrete wall retaining the soil of the approach berms (23.26636° 121.29767°)

5.1.4 *Dongli Railroad Bridge*

The Dongli Railroad Bridge (23.27795° 121.30666°) consists of 14 spans of pre-stressed concrete deck girders supported by pier foundations (Figures 23 and 24). The bridge exclusively carries rail traffic for the Taiwan Railways Taitung line. The longitudinal axis of the bridge is east to west, and the structure is perpendicular to the LVF and the direction of rupture. Major damage to the bridge was from the girders shifting on the pier caps damaging the railroad tracks and the structures supporting the powerline equipment to operate the trains. The use of shear keys, diaphragms, and other sacrificial elements prevented longitudinal or transverse unseating of the deck girders. During GEER's visit in October of 2022, the rail service had been suspended, and the bridge was being repaired with the target restoration of service prior to the Lunar new year (January 22, 2023). The ongoing repairs to the bridges, partially shown in Figure 5.23, were to reseat the bridge girders on elastomeric bearing pads and align adjacent spans vertically and horizontally.

At the ends of the pier elements were concrete bumper shear keys to constrain the bridge girders on the pier caps from transverse movement (Figure 5.25). These sacrificial elements reduced the lateral movement of the bridge girders, but each span had differential movement at adjacent spans because the bumpers could not completely prevent movement (Figures 24 and 25). Located on both outer edges of the pier caps between two adjacent spans were concrete structures supporting the overhead powerlines used to power the trains. Figure 5.26 is an image from a Google Street view of a typical powerline support structure and the narrow gap to the edge of the bridge deck. Following the failure of the concrete bumper shear keys, the bridge deck laterally loaded the powerline support structures, and the structures were not designed for those

lateral loads. Hence, 27 out of the 30 powerline structure supports were destroyed and needed replacement (Figures 23 and 24).

Figure 5.23. View of the Dongli Railroad Bridge during active repair operations. (23.27487° 121.30530°)

Figure 5.24. View from the bridge deck of the Dongli Railroad Bridge with the train rails removed. The twist in the deck was due to the lateral translation of the prestressed girders. (23.27829° 121.30669°)

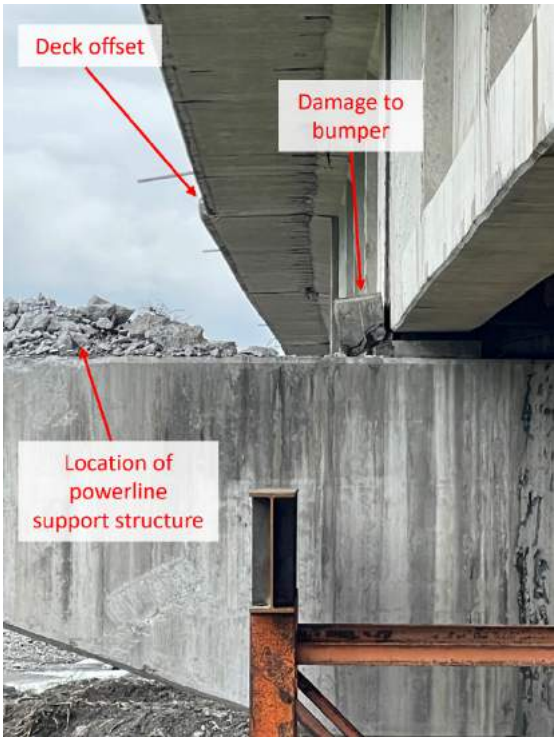

Figure 5.25. Typical damage to a concrete bumper shear key, offset of bridge deck, and location of concrete powerline support structure. (23.27481° 121.30502°)

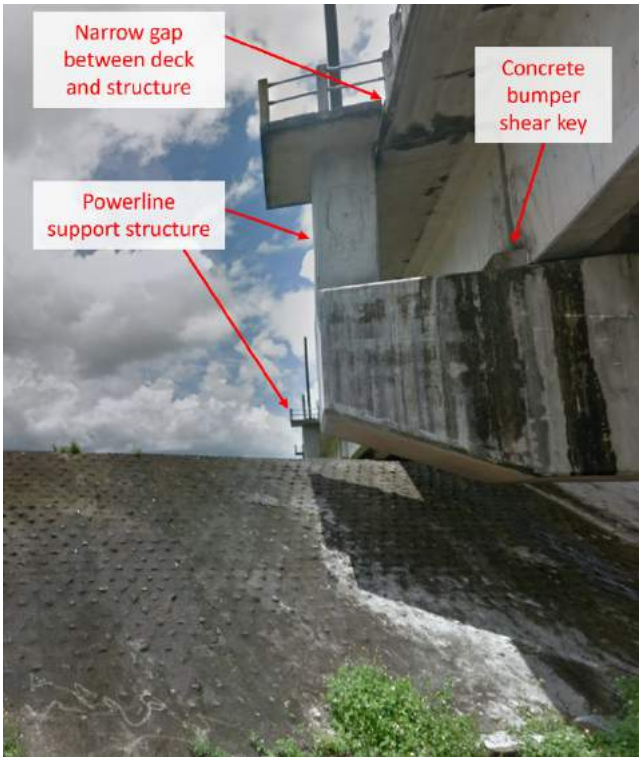

Figure 5.26. Google Street view from 2012 showing the intact powerline support structure and concrete bumper shear key (23.27468°, 121.30489°)

5.1.5 *Yuli Bridges (North bridge built in 1977 and South bridge in 1994)*

The Yuli bridges (23.32282° 121.32944°) are two parallel one-way automobile bridges near the Yuli township. The bridges are 575 m in length and consist of girders supported by pier foundations (Figures 27 and 28). Both bridges sustained minor damage, mainly near the abutments and at several expansion joints. During the GEER visit in October 2022, the south bridge was closed for repairs, and the north bridge was turned into a two-way bridge. The closure was for worker safety and not due to concerns about structural integrity. While the Yuli bridges were perpendicular to the LVF, the one unique difference of these bridges compared to the others described in this report is they were designed to span the suture of the Eurasian Plate and Philippine Sea Plate. Included in this design were elements to accommodate ongoing creep and permanent offset from a subduction zone earthquake.

The damage to the abutments appeared to be from pounding forces between the girders and the back wall of the abutment. Pounding damage caused the cracking and spalling in the abutment walls (Figure 5.29), damage to roadway approach slabs, which had subsequently been repaired, and rupture of utility lines.

The main source of damage at the expansion joints was the pounding of the concrete guardrail when the joints closed (Figure 5.30) or the differential movement to cause the misalignment of finger joints. The finger joint in Figure 5.31 was offset between 0.6 and 1.27 cm over the width of the travel lane. Due to access constraints, the GEER team was unable to survey below the deck to establish the source of the differential movement. Like the Dongli Railroad Bridge, the Yuli bridges had concrete bumper shear keys to constrain the bridge girders on the pier caps. At the mid-spans of the bridges, several of the bumpers were damaged and in need of repair or replacement. However, the bridge girders did not significantly translate on the pier caps, which would have resulted in damage to the finger joints or misalignment of the roadway.

Figure 5.27. View from the west abutment of the south Yuli bridge. (23.32332° 121.32684°)

Figure 5.28. View of the substructure of the North Yuli bridge. Similar structural components on the south bridge. (23.32320° 121.32780°)

Figure 5.29. Damage to the North Yuli bridge east abutment and adjacent utility lines. (23.32233° 121.33240°)

Figure 5.30. Typical damage in concrete railing at finger joints. (23.32317° 121.32758°)

Figure 5.31. Typical differential movement at a Figure 5.joint. (23.32240°121.33194°)

5.1.6 *Gaoliao Bridge (Built in 1991)*

The Gaoliao Bridge (23.38557° 121.34313°) is an 879 m long bridge with 22 spans of prestressed, precast concrete girders supported by pier foundations. The bridge orientation was east to west and perpendicular to the LVF and the direction of rupture. The Gaoliao bridge sustained the heaviest damage of the bridges surveyed, with 21 of the 22 spans and 20 of the 21 piers failing (Figures 32 and 33). Additionally, both built-up earthen abutment approaches sustained heavy damage and require extensive repairs or replacement. Upon the GEER team's arrival in October 2022, the concrete decks had been removed, leaving the damaged piers and bridge abutments (Figure 5.34).

The failure of the bridge piers in the Gaoliao Bridge was partially attributed to the formation of plastic hinges (Figure 5.34) and not global rotational failure like in the Lutain Bridge (Figures 6-14). The columns supporting the pier caps were 196 cm in diameter and varied in height between different spans. The longitudinal reinforcing of the columns was number #10 bars, spaced nominally at 19 cm, but spacing varied between bars and columns. These variations in bar spacing may have been as constructed or the reinforcement may have splayed when the plastic hinges formed. Spaced at 35 cm along longitudinal reinforcement was number 6 reinforcing hoops. Constant spacing of the hoops over the height of the column could not be verified because, above the plastic hinge, there was minimal spalling of the cover concrete. The GEER team did not observe any noticeable construction defects, such as cold joints or large aggregate particles in the failed piers. One of the pier failures near the east abutment is shown in Figure 5.35.

Both built-up earthen abutments on the east and west approaches had failures that caused wide and deep cracks in the roadway and settlements of 1-2 meters in some locations (Figures 36-44). The approaches were back-to-back concrete gravity walls backfilled with granular soils. The gravity walls had typical widths of about 30 cm at the top near the roadway and expanded 200

cm or wider at the native ground surface. Visually the particle sizes of the backfilled soil ranged from fine sands to rounded large cobbles, with the soil likely sourced from the nearby river. Indicators of global instability (e.g., bearing failures or rotational failures) were not identified at either of the approach abutments. Liquefaction likely did not trigger in the retained backfill because approaches were above the groundwater table, and there was sufficient drainage in the walls to prevent the retention of water behind the walls.

West Abutment: Larger cracks developed in the roadway near the double yellow line (Figure 5.36). At the southern gravity wall of the back-to-back system, the road had subsided nearly 1 m from the original location (Figure 5.37). The gravity wall did not have any major cracks or noticeable rotations, which may have precipitated the failure of the roadway. Along the north gravity wall damage, was less severe with little to no roadway racks. However, the foundations of the lighting along the edge of the concrete barriers raised 31 cm above the roadway (Figure 5.38).

East Abutment: The damage to the west approach was more extensive than the east. Figures 39 and 40 are drone images showing the damage from east and west. The cracks in the roadway were wider and deeper than the West abutment, and there was a partial failure of the gravity wall causing the road and backfill to spill into an adjacent rice field. Both the north and south back-to-back gravity walls translated laterally causing the roadway to settle from the original location (Figures 41 and 42). Near the center of the built-up approach was a tunnel for access between the adjacent rice fields. The tunnel was secured to the ground and not to the concrete gravity walls, and the walls could move independently from the original location of the tunnel. The North concrete gravity wall translated away from the tunnel by approximately 41 cm, with a similar offset at the south wall (Figure 5.43). These translations may be a potential cause for the roadway settlement of 1 m.

As noted earlier the backfill soil of the approaches ranged in particle sizes from sands to cobbles (Figure 5.44). At soil at the locations of the roadway cacks the soil was dense and was difficult to break apart. However, when the gravity wall moved relative to the tunnel, a gap opened exposing the soil, and at the largest gap around the tunnel, the soil flowed from this open crack (Figure 5.43). This soil piled up on the ground and caused a sinkhole on the roadway surface. While the soil near the roadway surface may have been subjected to mechanical compaction energy or traffic loading, the soil with increasing depth from the ground surface may be loose enough to be flowable.

Figure 5.32. Failed spans of the Gaoliao bridge looking west (Image courteous of Zola Zhou, 23.38563° 121.34458°)

Figure 5.33. Failed spans of the Gaoliao bridge looking east (Image courteous of Zola Zhou, 23.38563° 121.34458°)

Figure 5.34. Looking towards the east abutment at the failed piers (23.38632° 121.33973°)

Figure 5.35. Typical view of the plastic hinges in the concrete piers (23.38630° 121.33930°)

Figure 5.36. Roadway cracks and settlement in west abutment. Note (23.38625° 121.33806°)

Figure 5.37. Roadway settlement at the south back-to-back concrete gravity wall in the west abutment (23.38629° 121.33811°)

Figure 5.38. Settlement near the light post foundation in the east abutment (23.38617° 121.33741°)

Figure 5.39. Drone view of the east abutment looking east (approx. 23.38522° 121.34690°)

Figure 5.40. Drone view of the east abutment looking west (approx. 23.38481° 121.34911°)

Figure 5.41. Roadway cracks and settlement in the east abutment looking east (23.38520° 121.34710°)

Figure 5.42. Roadway cracks and settlement in the east abutment looking west (23.38510° 121.34767°)

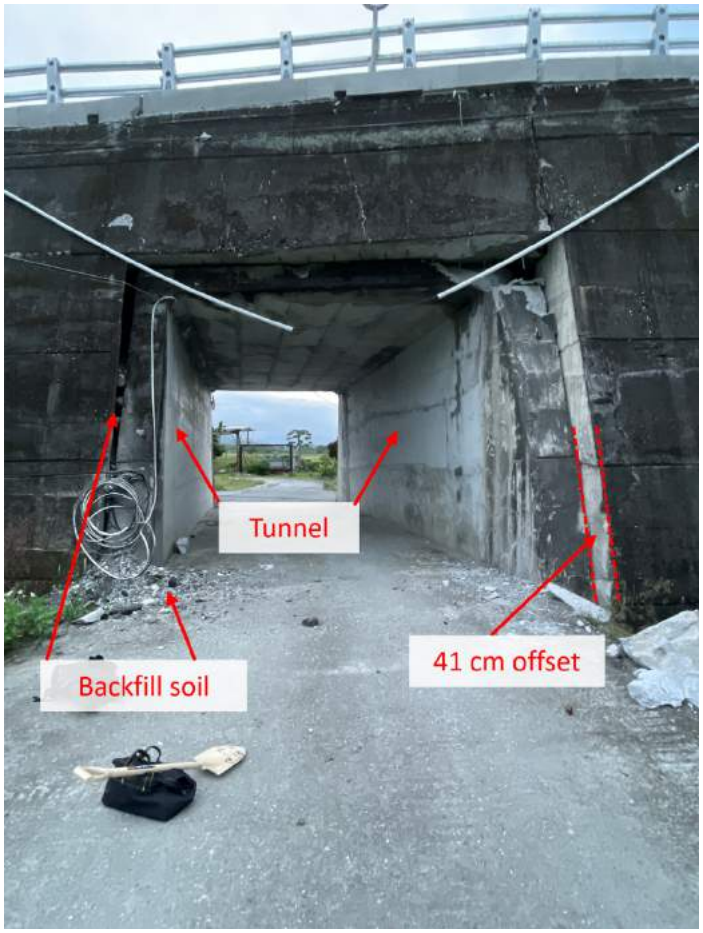

Figure 5.43. Tunnel beneath east bridge approach, 41 cm offset from gravity wall, and backfill soil that flowed from gap between the gravity wall and tunnel liner (23.38526° 121.34783°)

Figure 5.44. Typical profile of backfilled soils (23.38509° 121.34773°)